

Accelerated Article Preview

Signatures of chiral superconductivity in rhombohedral graphene

Received: 1 September 2024

Accepted: 16 May 2025

Accelerated Article Preview

Published online: 22 May 2025

Cite this article as: Han, T. et al. Signatures of chiral superconductivity in rhombohedral graphene. *Nature* <https://doi.org/10.1038/s41586-025-09169-7> (2025)

Tonghang Han, Zhengguang Lu, Zach Hadjiri, Lihan Shi, Zhenghan Wu, Wei Xu, Yuxuan Yao, Armel A. Cotten, Omid Sharifi Sedeh, Henok Weldeyesus, Jixiang Yang, Junseok Seo, Shenyong Ye, Muyang Zhou, Haoyang Liu, Gang Shi, Zhenqi Hua, Kenji Watanabe, Takashi Taniguchi, Peng Xiong, Dominik M. Zumbühl, Liang Fu & Long Ju

This is a PDF file of a peer-reviewed paper that has been accepted for publication. Although unedited, the content has been subjected to preliminary formatting. Nature is providing this early version of the typeset paper as a service to our authors and readers. The text and figures will undergo copyediting and a proof review before the paper is published in its final form. Please note that during the production process errors may be discovered which could affect the content, and all legal disclaimers apply.

Signatures of chiral superconductivity in rhombohedral graphene

Tonghang Han^{1†}, Zhengguang Lu^{1,2†}, Zach Hadjri^{1†}, Lihan Shi¹, Zhenghan Wu¹, Wei Xu¹, Yuxuan Yao¹, Armel A. Cotten³, Omid Sharifi Sede³, Henok Weldeyesus³, Jixiang Yang¹, Junseok Seo¹, Shenyong Ye¹, Muyang Zhou¹, Haoyang Liu², Gang Shi², Zhenqi Hua², Kenji Watanabe⁴, Takashi Taniguchi⁵, Peng Xiong², Dominik M. Zumbühl³, Liang Fu¹, Long Ju^{1*}

¹Department of Physics, Massachusetts Institute of Technology, Cambridge, MA, 02139, USA.

²Department of Physics, Florida State University, Tallahassee, FL, 32306, USA

³Department of Physics, University of Basel, 4056, Basel, Switzerland

⁴Research Center for Electronic and Optical Materials, National Institute for Materials Science, 1-1 Namiki, Tsukuba 305-0044, Japan

⁵Research Center for Materials Nanoarchitectonics, National Institute for Materials Science, 1-1 Namiki, Tsukuba 305-0044, Japan

*Corresponding author. Email: longju@mit.edu †These authors contributed equally to this work.

Chiral superconductors are unconventional superconducting states that break time reversal symmetry spontaneously and typically feature Cooper pairing at non-zero angular momentum. Such states may host Majorana fermions and provide an important platform for topological physics research and fault-tolerant quantum computing¹⁻⁷. Despite intensive search and prolonged studies of several candidate systems⁸⁻²⁶, chiral superconductivity has remained elusive so far. Here we report the discovery of robust unconventional superconductivity in rhombohedral tetra- and penta-layer graphene without moiré superlattice effects. We observed two superconducting states in the gate-induced flat conduction bands with T_c up to 300 mK and charge density n_e down to $2.4 \times 10^{11} \text{ cm}^{-2}$ in five devices. Spontaneous time-reversal-symmetry-breaking due to electron's orbital motion is found, and several observations indicate the chiral nature of these superconducting states, including: 1. In the superconducting state, R_{xx} shows magnetic hysteresis in varying out-of-plane magnetic field B_\perp —absent from all other superconductors; 2. the superconducting states are robust against in-plane magnetic field and are developed within a spin- and valley-polarized quarter-metal phase; 3. the normal states show anomalous Hall signals at zero magnetic field and magnetic hysteresis. We also observed a critical B_\perp of 1.4 Tesla, higher than any graphene superconductivity and indicates a strong-coupling superconductivity close to the BCS-BEC crossover²⁷. Our observations establish a pure carbon material for the study of topological superconductivity, with the promise to explore Majorana modes and topological quantum computing.

32

33

34 Topological superconductivity has been conceived as new quantum states of matter, which host exotic
35 quasiparticles that have great potential applications in quantum computing^{1,2,4-7}. Chiral superconductors
36 could host topological superconductivity with time-reversal-symmetry-breaking (TRSB) and magnetic
37 hysteresis^{2-4,6,28}. Several candidates of chiral superconductors have been investigated through a variety of
38 experimental techniques since three decades ago^{8-24,26}. Although signatures that are compatible with chiral
39 superconductivity have been identified, most recent experimental reports suggest alternative pictures. For
40 example, UTe₂ and Sr₂RuO₄ have been shown to have single-component order parameters that is
41 incompatible with chiral superconductivity^{16,29,30}, and alternative origins of the observed TRSB were
42 suggested³¹. In all these superconductors, there has been no evidence of anomalous Hall effect or magnetic
43 hysteresis in their charge transport, making chiral superconductivity an elusive goal to be realized.

44 Graphene-based two-dimensional material heterostructures have emerged as a new playground for
45 superconductivity with unconventional ingredients. By introducing the moiré superlattice between adjacent
46 graphene layers, or between graphene and hBN, superconducting and correlated insulating states have been
47 observed, reminiscent of the phase diagram of high- T_c superconductors (Methods). More recently, it was
48 shown that crystalline graphene in the rhombohedral stacking order could also exhibit superconductivity in
49 the absence of moiré effects (Methods). Rhombohedral stacked multilayer graphene hosts gate-tunable flat
50 bands which drastically promotes correlation effects^{32,33}. As shown in Fig. 1b, the conduction band in tetra-
51 layer graphene becomes most flat when a gate-induced interlayer potential difference (between the top-
52 most and bottom-most graphene layers) $\Delta = 90$ meV, based on our tight-binding calculation (see Methods).
53 Similar scenario happens in pentalayer graphene. As a result, various ground states with broken spin and/or
54 valley symmetries due to the exchange interactions have been observed (Methods). Such states with tunable
55 fermi-surface topology and various spin/valley characters provide a fertile ground to search for
56 unconventional superconductivity^{34,35}, including chiral superconductivity. Especially, interaction-induced
57 valley polarization results in TRSB due to the chirality of electron motion, while the valley-dependent
58 pseudo-spin winding^{32,33,36} and angular-momentum³⁷ might facilitate high-angular-momentum pairing
59 between electrons. The search of superconductivities in rhombohedral graphene, however, has been limited
60 to three layers so far (Methods), and the potential of unconventional superconductivity in this system is yet
61 to be fully explored.

62 Here we report the DC transport study of rhombohedral stacked tetra- and penta-layer graphene
63 devices. We observed superconductivity on the electron-doped side with the highest transition temperature
64 of 300 mK. We measured three tetralayer and two pentalayer devices: Device T1 is tetra-layer graphene
65 with electrons close to WSe₂, Device T2 is tetra-layer graphene with electrons away from WSe₂, Device T3
66 is bare tetra-layer graphene without WSe₂, Device P1 and P2 are bare penta-layer. All five devices show
67 two unconventional superconducting states, in the absence of a detectable moiré superlattice. Several
68 observations indicate TRSB and valley polarization in the observed superconducting states, most notably
69 magnetic hysteresis in both the superconducting state and its corresponding normal state. These
70 superconducting states persist to an out-of-plane magnetic field B_{\perp} up to 1.4 Tesla – indicating a
71 superconducting coherence length close to the inter-electron distance, and the underlying strongly coupled
72 superconductivity picture^{27,38}. We will focus on Device T3 and P1 in the main text, since there is no WSe₂
73 in them and the discussion is simpler. The data from Device T1, T2 and P2 are included as Extended Data
74 Figures (T1: Fig.7-8, T2: Fig.1-3, P2: Fig.10), where the influence of WSe₂ will also be discussed.

75 **Phase diagram showing superconductivity**

76 Figure 1c shows the longitudinal resistance R_{xx} map at the nominal base temperature of 7 mK at the mixing
77 chamber, when Device T3 is electron-doped in the flat conduction band. At around $D/\varepsilon_0 = 1.1$ V/nm, three
78 regions show vanishing resistances, as pointed by the arrows. Similar phase diagram is observed in Device
79 P1 as shown in Fig. 1d, featuring three regions of vanishing resistances alike those in Device T3. We note
80 that SC3 in Device P1 is not well-developed, while in Device P2 it is well-developed (see Extended Data
81 Fig. 10). We name these three regions as SC1-3, since they are all superconducting states (see more data in
82 Extended Data Figs. 4&9). Figure 1e&f show the temperature dependence of R_{xx} in SC1-SC3. All three
83 states show a transition to zero R_{xx} as the temperature is lowered. The transition temperature reaches ~ 300
84 mK for SC1 in Device T3, highest among all superconducting states in Device T3 and P1. There is another
85 superconducting SC4 state at high-electron-doping observed in Device T2 that is phenomenologically
86 different from the superconductivity shown in Fig. 1c&d, especially SC1&2 (see Extended Data Figure 1).

87 SC1-3 reside at $n_e < 10^{12}$ cm⁻², corresponding to all the electrons located in the flat band bottom as
88 shown in Fig. 1b at $\Delta = 90$ mV, assuming the electrons are of the same spin and valley characters like in a
89 quarter-metal. At the same time, SC1-3 are neighbored by a highly resistive region at lower densities, which
90 is also reminiscent of the highly resistive region in tetra- to hexa-layer rhombohedral graphene/hBN moiré
91 superlattices (Methods). These observations of SC1-3 are in line with the expectation of strong electron
92 correlation effects happening in the flat conduction band at intermediate D , as that is shown in Fig. 1b.

93 Neighboring quarter-metal state

94 To understand the superconductivities shown in Fig. 1 better, we first characterize the neighboring metallic
95 states. We use the tetralayer Device T3 as an example, while the observations in the pentalayer Device P1
96 is similar (see Extended Data Figure 9). Figure 2a&b show the R_{xx} and R_{xy} maps taken at $B_\perp = 0.1$ T and the
97 base temperature, in which the SC1 and SC2 regions can be clearly seen with vanishing values in both
98 maps. SC3 is no longer visible in these maps, indicating an out-of-plane critical magnetic field less than 0.1
99 T. Furthermore, Fig. 2c shows the magnetic field scans taken in the states indicated by the purple and blue
100 dots in Fig. 2b, respectively, revealing hysteretic loops in R_{xx} and R_{xy} . Fig. 2d shows the R_{xx} map taken at
101 $B_\perp = 1$ T. The region neighboring the high-density boundary of SC1 and the low- D boundary of SC2 shows
102 clear quantum oscillations with a period that corresponds to that of a quarter-metal (Methods). We did not
103 observe quantum oscillations in the regions of SC1&2, possibly due to the extremely large effective mass
104 and small cyclotron gap corresponding to the flat electron band in these regions (see Extended Data Figure
105 12).

106 The anomalous Hall signals and magnetic hysteresis shown in Fig. 2c clearly indicate a spontaneous
107 valley polarization and TRS-breaking. Together with the quantum oscillation data in Fig. 2d, we conclude
108 that SC1 and SC2 are neighbored by spin- and valley-polarized quarter-metals. The TRS is broken at the
109 orbital level in these quarter-metal states, and the system spontaneously chooses a chirality in its electron
110 transport at zero magnetic field due to the valley-polarization.

111 After establishing that spin- and valley-polarized quarter-metals are neighboring SC1 and SC2, we
112 proceed to explore the evolution of the three states in magnetic field. Fig. 2e&f show the R_{xx} and R_{xy} taken
113 along the dashed lines in Fig. 2a&b as a function of B_\perp . At this D , SC1 can persist to ~ 0.6 T before the R_{xx}
114 value starts to deviate from zero. The phase boundary between SC1 and the valley-polarized quarter-metal
115 remains at the same n_e as B_\perp is increased. The left boundary even expands to lower density from $B_\perp = 0$ to
116 0.4 T, meaning that states in a small range of n_e become superconducting only under a non-zero B_\perp .

117 The critical magnetic field of > 0.6 T in tetralayer graphene is unusually high for graphene
118 superconductivity, and the corresponding value in the pentalayer device can even reach 1.4 T. We will
119 discuss them in detail in Fig. 5. For now, we focus on the competition between SC1 and the neighboring
120 states. If SC1 has zero orbital magnetization (or non-zero but smaller than that of the spin- and valley-
121 polarized QM), the range of SC1 will shrink upon the application of B_{\perp} , since the energy of the QM will be
122 lowered more than that of SC1 will be (Methods). The observation of SC1 holding against the neighboring
123 quarter-metal and even expanding implies the valley-polarization and orbital magnetic nature of SC1.

124 **Spin-valley-polarized superconductivity**

125 Knowing the spin- and valley-polarized QM nature of the neighboring metallic states, next we directly
126 probe the spin and valley symmetry in SC1&2. Here we use data from the pentalayer Device P1 as an
127 example. Figure 3a-d show the n_e - D maps of R_{xx} at in-plane magnetic field $B_{\parallel} = 0, 1, 3, 5$ T, respectively
128 (an out-of-plane magnetic field $B_{\perp} = 0.2$ T is applied to prevent the random fluctuation of R_{xx} , see Methods
129 for discussion). Under an in-plane magnetic field, the zero-resistance of superconducting state survives in
130 most of the SC1 region that was shown at zero magnetic field. Similar observation is made for SC2, as
131 shown in Fig. 3e-h.

132 The robust superconductivity in a large in-plane magnetic field indicates the spin-polarized nature
133 of SC1 and SC2. The Pauli-limit-Violation-Ratio (PVR) is already ~ 15 for SC1 at 5 T (see Methods), and
134 the true PVR is likely much larger than 15, should we increase the magnetic field to even higher values to
135 test. The lower limits of the in-plane critical field we observed is larger than in the spin-polarized
136 superconductivity in bilayer graphene (Methods). The spin-polarization of SC1 and SC2 indicates the
137 connection between these superconducting states and the neighboring QM.

138 Figure 3i&j show the R_{xx} under scanned B_{\perp} in SC1 and SC2, respectively. Surprisingly, clear
139 hysteresis between two zero-resistance states is observed for both superconductivities. A non-zero-
140 resistance peak appears during the scanning, the magnetic field at which shows a hysteresis between
141 forward and backward scans. Furthermore, such non-zero-resistance peak between zero-resistance states
142 and the hysteresis behavior are observed even when a large in-plane magnetic field B_{\parallel} is applied, as shown
143 in Fig. 3k&l.

144 The magnetic hysteresis of resistance in a superconducting state is highly unusual and distinct from
145 all other superconductors: ferromagnetic superconductors show magnetic hysteresis in their optical
146 responses but not in resistance directly³⁹; magnetic hysteresis in resistance due to vortex-array-melting
147 happen between the superconducting and metallic states⁴⁰, rather than between two superconducting states.
148 The observations in Fig. 3i-l suggest the orbital magnetic nature of SC1 and SC2. This is illustrated in Fig.
149 3m: the two zero-resistance states at large B_{\perp} field correspond to a single (and opposite-) valley-polarized
150 domain between the voltage contacts in the device, while the non-zero resistance during scanning happens
151 when a domain wall separates opposite-valley-polarized domains. This domain is expected to be resistive,
152 as the tunneling of Cooper pair through it does not conserve momentum. The domain is flipped due to the
153 coupling of valley-orbital-magnetization and the out-of-plane magnetic field—a mechanism similar to that
154 induces the hysteresis shown in Fig. 2c. The possibility of domain flipping due to coupling to the spin
155 magnetization is ruled out in two ways: 1. in Fig. 3k&l, the spin is always locked to the in-plane direction
156 during scanning due to the much larger B_{\parallel} field than B_{\perp} field; 2. when the valley polarization is fixed by a
157 B_{\perp} field, scanning the B_{\parallel} field in a large range does not induce any non-zero-resistance state or hysteresis,

158 as shown in Fig. 3n&o. These observations strongly suggest the similarity and connection between the spin-
159 valley-polarized QM and SC1&2 (see Extended Data Figure 5).

160 Temperature-dependent phase evolution

161 Another approach to understand the SC1&2 as well as their relation with the neighboring QM is to explore
162 the corresponding normal states. Here we focus on data from the tetralayer Device T3 for the most complete
163 characterization. The behaviors in other devices are qualitatively the same (see Extended Data Figures 3&9
164 for example). Figure 4a&b show the symmetrized R_{xx} and anti-symmetrized R_{xy} maps respectively at $B_\perp =$
165 0.1 T and $T = 480$ mK. The zero resistances in both SC1 and SC2 are replaced by values that are around 1-
166 2 k Ω . In the Hall resistance map Fig. 4b, anomalous Hall signals of ~ 100 Ω are distributed in a region that
167 overlaps with the SC1 and SC2 regions (outlined by the dashed oval-shaped curves). These anomalous Hall
168 signals are confirmed by Fig. 4c, where the R_{xy} at scanned magnetic fields are shown for representative n_e -
169 D combinations both within SC1 and in surrounding states (corresponding to the five symbols in Fig. 4b).
170 Such magnetic hysteresis persists to 7 mK while R_{xy} is zero in SC1 except for at the coercive fields, as
171 shown in Fig. 4d. Figure 4e shows the evolution of R_{xy} hysteresis as a function of temperature at the star
172 position.

173 These observations suggest that the TRSB and valley-polarization already exist in the normal states
174 of superconducting SC1 and SC2 states. To our knowledge, this is the first time that an anomalous Hall
175 signal at zero magnetic field and magnetic hysteresis behavior are observed in the normal state of a
176 superconductor, except for in hybrid systems where superconductivity and ferromagnetism co-exist^{39,41-43}.
177 These features are inherited by the electrons when they become superconducting at below the transition
178 temperature. The Hall angles in these anomalous Hall states are quite large, corresponding to $\tan\theta_H = \frac{R_{xy}}{R_{xx}} \sim$
179 up to 0.1, which is typical for quarter-metal states in crystalline rhombohedral graphene devices (Methods).

180 We note that there is a clear boundary intercepting the SC1 region in Fig. 4a, which corresponds to
181 a sudden change of R_{xx} . This boundary is highlighted by the orange dashed curve in Fig. 4f. At a specific
182 displacement field ($D/\epsilon_0 = 0.923$ V/nm for example, as shown in Fig. 4g), this phase boundary and kink in
183 R_{xx} gradually shift to lower n_e during cooling down. At ~ 250 mK, the SC1 dome starts to develop in the
184 region that is on the higher-density-side of this phase boundary. Figure 4h shows line-cuts at varying
185 temperatures that highlight the kink and its temperature-dependent evolution.

186 By performing quantum oscillation measurements, we determine the higher-density-side of this
187 boundary to be the spin- and valley-polarized quarter metal. It is hard to determine the Fermi surface
188 topology of the lower-density-side due to the lack of clear quantum oscillations (we thus name it
189 ‘undetermined metal’ or ‘UM’), while one possibility is a metal state with annular Fermi surface and full
190 spin and valley polarizations (see Extended Data Figure 6 for details). Although at 480 mK the QM-UM
191 phase boundary intercepts the SC1 region, the same phase boundary gradually shifts to lower n_e and
192 eventually enclose the entire SC1 region into the QM phase. This observation indicates that the SC1 state
193 develops from the spin- and valley-polarized QM parent state.

194 Strong coupling of Cooper pairing

195 Lastly, we explore the out-of-plane magnetic-field-dependence of SC1-SC3 in greater details. Figure 5a&b
196 show the R_{xx} in SC1-3 states as a function of B_\perp in the tetra- and pentalayer devices, respectively. In both
197 cases, one can see that R_{xx} deviates from zero as B_\perp is increased. We define the critical magnetic field $B_{\perp,c}$

198 as the field when the R_{xx} reaches 10% of the normal state resistance and its uncertainty as the field range
199 between 5% and 15% (see Extended Data Fig. 9), and extract the phenomenological Ginzburg-Landau
200 superconducting coherence length as $\xi_{GL} = \left(\frac{\Phi_0}{2\pi B_{\perp,c}}\right)^{\frac{1}{2}}$, where $\Phi_0 = \frac{\hbar}{2e}$ is the superconducting magnetic flux
201 quantum. Remarkably, R_{xx} in SC1 in the pentalayer device remains within the noise level until $B_{\perp} = 1.4$ T.
202 Figure 5c summarizes the ξ_{GL} as a function of n_e for SC1-3 at representative displacement fields. As a
203 reference, we plot the inter-electron distance $d_{\text{particle}} = n_e^{-1/2}$ determined by the charge density n_e ³⁸. The
204 coherence length in SC3 is well-above the inter-electron distance. However, the coherence length in SC1
205 and SC2 are much closer to the latter, especially SC1 in the pentalayer device.

206 The observations show that SC1 is very unusual that the electrons have a much stronger coupling
207 strength. SC1 is already close to the BCS-BEC crossover²⁷, although still mainly residing on the BCS side.
208 We note that the critical magnetic field $B_{\perp,c}$ observed in our pentalayer device is higher than any graphene-
209 based superconductors, crystalline or twisted. Compared to the superconducting state in twisted tri-layer
210 graphene³⁸, the T_c of SC1 in our experiment is more than 10 times lower, but the electron density at which
211 superconductivity is observed is similar, while the critical magnetic field $B_{\perp,c}$ is 2-3 times higher.

212 Discussion

213 To summarize, we observed two superconducting states SC1 and SC2 that exhibit unusual properties: 1.
214 Magnetic hysteresis and orbital magnetism in the superconducting states; 2. SC1 develops within a spin-
215 and valley-polarized quarter-metal phase, and is robust against the remaining QM state under an out-of-
216 plane magnetic field; 3. the non-zero anomalous Hall signals at zero magnetic field and clear magnetic
217 hysteresis at temperatures above T_c . These observations clearly suggest unconventional superconductivity
218 that is distinct from any existing superconductors. These observations suggest spontaneous TRSB at the
219 orbital level in the superconducting states, which is the defining feature of chiral superconductivity^{2-4,6}.

220 Microscopically, our observations indicate a spin- and valley-symmetry-broken parent state of
221 superconductivity in SC1, and a valley-symmetry-broken parent state of SC2. In SC1, the parent state is a
222 fully spin- and valley-polarized quarter-metal, which has only one pocket at the Fermi level. In SC2, the
223 parent state is likely a metal state with an annular Fermi surface, which might even have occupations in two
224 different-sized pockets located in opposite valleys (which may have full or partial spin/valley polarization).
225 In the quarter metal case, Cooper pairing occurs within same spin states in a single valley, which must have
226 odd angular momentum due to Pauli exclusion principle, e.g., p-wave or f-wave. Due to the presence of
227 Berry curvature in the valley-polarized state as evidenced by the anomalous Hall effect above T_c , we expect
228 the complex-valued chiral order parameter such as $p+ip$ is favored over the real order parameter such as p_x .
229 Such chiral superconductors with a single non-degenerate Fermi pocket in two dimensions may be
230 topologically nontrivial and host localized Majorana modes in the vortex core and chiral Majorana fermions
231 at the boundary². We also note that intravalley pairing leads to a large Cooper pair momentum, thus
232 realizing a finite-momentum superconductor^{24,25,44-46}. We note that in roughly the same n_e - D range hosting
233 SC1-3, tetra- to hexa-layer rhombohedral graphene/hBN moiré superlattice devices show fractional
234 quantum anomalous Hall effects that are hosted by a valley- and spin-polarized topological flat band
(Methods).

236 Our experiment demonstrates a new platform based on simple crystalline graphene for exploring
237 topological superconductivity with local and chiral Majorana zero modes¹⁻⁷. To understand the

superconducting ground states that we have observed, future experiments may be performed in several exciting directions: 1. directly probing the TRSB and the orbital magnetism in the superconducting state by using Kerr rotation optical spectroscopy⁴⁷ or scanning SQUID^{43,48,49}; 2. determining the superconducting gap symmetry by measuring the Fraunhofer pattern of in-plane Josephson junctions^{50,51} or Little-Parks effect⁵²; 3. characterizing the distribution of supercurrent in magnetic field^{53,54} and/or by directly imaging the possible persistent edge current by scanning SQUID⁴⁸; 4. testing quantized thermal conductance of possible Majorana chiral modes on the edges⁵⁵. Our experiment opens up new directions in superconductivity and electron topology physics, and could pave the way to non-abelian-quasi-particle engineering for topologically protected quantum computation applications.

247

248 Main Text References

- 249 Sato, M. & Ando, Y. Topological superconductors: a review. *Rep. Prog. Phys.* **80**, 076501 (2017).
- 250 N Read, D. G. Paired states of fermions in two dimensions with breaking of parity and time-reversal
251 symmetries and the fractional quantum Hall effect. *Phys. Rev. B* **61**, 10267–10297 (2000).
- 252 C Kallin, J. B. Chiral superconductors. *Rep. Prog. Phys.* **79**, 054502 (2016).
- 253 X-L Qi, S.-C. Z. Topological insulators and superconductors. *Rev. Mod. Phys.* **83**, 1057–1110 (2011).
- 254 Kitaev, A. Periodic table for topological insulators and superconductors. *AIP Conf Proc* **1134**, 22–30
255 (2009).
- 256 Nayak, C., Simon, S. H., Stern, A., Freedman, M. & Das Sarma, S. Non-Abelian anyons and topological
257 quantum computation. *Rev Mod Phys* **80**, 1083–1159 (2008).
- 258 Schnyder, A. P., Ryu, S., Furusaki, A. & Ludwig, A. W. W. Classification of topological insulators and
259 superconductors in three spatial dimensions. *Phys Rev B* **78**, 195125 (2008).
- 260 Maeno, Y. *et al.* Superconductivity in a layered perovskite without copper. *Nature* **1994** *372*:6506 **372**,
261 532–534 (1994).
- 262 Ghosh, S. *et al.* Thermodynamic evidence for a two-component superconducting order parameter in
263 Sr₂RuO₄. *Nat. Phys.* **17**, 199–204 (2021).
- 264 Saxena, S. Superconductivity on the border of itinerant-electron ferromagnetism in UGe₂. *Nature* **406**,
265 587–592 (2000).
- 266 GR Stewart, Z. F. J. W. J. S. Possibility of coexistence of bulk superconductivity and spin fluctuations in
267 UPt₃. *Phys. Rev. Lett.* **52**, 679–682 (1984).
- 268 Aoki, D. Coexistence of superconductivity and ferromagnetism in URhGe. *Nature* **413**, 613–616 (2001).
- 269 Ran, S. *et al.* Nearly ferromagnetic spin-triplet superconductivity. *Science* (1979) **365**, 684–687 (2019).
- 270 Hayes, I. M. *et al.* Multicomponent superconducting order parameter in UTe₂. *Science* (1979) **373**, 797–
271 801 (2021).
- 272 Jiao, L. *et al.* Chiral superconductivity in heavy-fermion metal UTe₂. *Nature* **579**, 523–527 (2020).

- 276 Theuss, F. *et al.* Single-component superconductivity in UTe₂ at ambient pressure. *Nature Physics* 2024
274 20:7 **20**, 1124–1130 (2024).
- 275 R Nandkishore, L. L. A. C. Chiral superconductivity from repulsive interactions in doped graphene. *Nat.*
276 *Phys.* **8**, 158–163 (2012).
- 277 Ming, F. *et al.* Evidence for chiral superconductivity on a silicon surface. *Nature Physics* 2023 19:4 **19**,
278 500–506 (2023).
- 279 Wan, Z. *et al.* Unconventional superconductivity in chiral molecule–TaS₂ hybrid superlattices. *Nature*
280 (2024) doi:10.1038/S41586-024-07625-4.
- 281 Li, Z. *et al.* Observation of odd-parity superconductivity in UTe₂. *arXiv*: 2309.08668 (2023).
- 282 Mielke, C. *et al.* Time-reversal symmetry-breaking charge order in a kagome superconductor. *Nature*
283 **602**, 245–250 (2022).
- 284 Yin, J. X., Lian, B. & Hasan, M. Z. Topological kagome magnets and superconductors. *Nature* 2022
285 612:7941 **612**, 647–657 (2022).
- 286 Le, T. *et al.* Superconducting diode effect and interference patterns in kagome CsV₃Sb₅. *Nature* 2024
287 630:8015 **630**, 64–69 (2024).
- 288 Hsu, Y. T., Vaezi, A., Fischer, M. H. & Kim, E. A. Topological superconductivity in monolayer transition
289 metal dichalcogenides. *Nature Communications* 2017 8:1 **8**, 1–6 (2017).
- 290 Murshed, S. A., Szabó, A. L. & Roy, B. Nodal pair-density-waves from quarter-metal in crystalline
291 graphene multilayers. *arXiv*: 2210.15660 (2022).
- 292 Deng, H. *et al.* Evidence for time-reversal symmetry-breaking kagome superconductivity. *Nature*
293 *Materials* 2024 23:12 **23**, 1639–1644 (2024).
- 294 Randeria, M. & Taylor, E. Crossover from Bardeen-Cooper-Schrieffer to Bose-Einstein condensation and
295 the unitary Fermi gas. *Annu Rev Condens Matter Phys* **5**, 209–232 (2014).
- 296 Cheng, M., Sun, K., Galitski, V. & Das Sarma, S. Stable topological superconductivity in a family of two-
297 dimensional fermion models. *Phys Rev B Condens Matter Mater Phys* **81**, 024504 (2010).
- 298 Li, Y. S. *et al.* High-sensitivity heat-capacity measurements on Sr₂RuO₄ under uniaxial pressure. *Proc*
299 *Natl Acad Sci U S A* **118**, e2020492118 (2021).
- 300 Pustogow, A. *et al.* Constraints on the superconducting order parameter in Sr₂RuO₄ from oxygen-17
301 nuclear magnetic resonance. *Nature* 2019 574:7776 **574**, 72–75 (2019).
- 302 Willa, R., Hecker, M., Fernandes, R. M. & Schmalian, J. Inhomogeneous time-reversal symmetry breaking
303 in. *Phys Rev B* **104**, 024511 (2021).
- 304 Min, H. & MacDonald, A. H. Electronic structure of multilayer graphene. *Progress of Theoretical Physics*
305 *Supplement* **176**, 227–252 (2008).
- 306 Koshino, M. & McCann, E. Trigonal warping and Berry's phase $N\pi$ in ABC-stacked multilayer graphene.
307 *Phys. Rev. B* **80**, 165409 (2009).

- 308 Ghazaryan, A., Holder, T., Berg, E. & Serbyn, M. Multilayer graphenes as a platform for interaction-
309 driven physics and topological superconductivity. *arXiv*:2211.02492 (2022)
310 doi:10.48550/arxiv.2211.02492.
- 315 Viñas Boström, E. *et al.* Phonon-mediated unconventional superconductivity in rhombohedral stacked
312 multilayer graphene. *npj Computational Materials* 2024 10:1 **10**, 1–8 (2024).
- 316 Castro Neto, A. H., Guinea, F., Peres, N. M. R., Novoselov, K. S. & Geim, A. K. The electronic properties of
314 graphene. *Rev Mod Phys* **81**, 109–162 (2009).
- 315 Cao, T., Wu, M. & Louie, S. G. Unifying Optical Selection Rules for Excitons in Two Dimensions: Band
316 Topology and Winding Numbers. *Phys Rev Lett* **120**, 087402 (2018).
- 317 Park, J. M., Cao, Y., Watanabe, K., Taniguchi, T. & Jarillo-Herrero, P. Tunable strongly coupled
318 superconductivity in magic-angle twisted trilayer graphene. *Nature* 2021 590:7845 **590**, 249–255 (2021).
- 319 Yi, H. *et al.* Interface-induced superconductivity in magnetic topological insulators. *Science* (1979) **383**,
320 634–639 (2024).
- 321 Safar, H. *et al.* Experimental evidence for a first-order vortex-lattice-melting transition in untwinned,
322 single crystal YBa₂Cu₃O₇. *Phys Rev Lett* **69**, 824 (1992).
- 323 Hu, Y., Meng, F., Lei, H., Xue, Q.-K. & Zhang, D. Possible spin-polarized Cooper pairing in high
324 temperature FeSe superconductor. *arXiv*: 2405.10482 (2024).
- 325 Ma, L. *et al.* Electric-field-controlled superconductor–ferromagnetic insulator transition. *Sci Bull (Beijing)*
326 **64**, 653–658 (2019).
- 327 Bert, J. A. *et al.* Direct imaging of the coexistence of ferromagnetism and superconductivity
328 at the LaAlO₃/SrTiO₃ interface. *Nature Physics* 2011 7:10 **7**, 767–771 (2011).
- 329 Fulde, P. & Ferrell, R. A. Superconductivity in a strong spin-exchange field. *Phys. Rev.* **135**, 550 (1964).
- 330 Larkin, A. I. ; O. Yu. N. Inhomogeneous state of superconductors. *Sov. Phys. JETP* **20**, 762–769 (1965).
- 331 Casalbuoni, R. & Nardulli, G. Inhomogeneous superconductivity in condensed matter and QCD. *Rev Mod
332 Phys* **76**, 263 (2004).
- 333 Charbonneau, P. *et al.* Polar Kerr effect as probe for time-reversal symmetry breaking in unconventional
334 superconductors. *New J Phys* **11**, 055060 (2009).
- 335 Uri, A. *et al.* Nanoscale imaging of equilibrium quantum Hall edge currents and of the magnetic
336 monopole response in graphene. *Nature Physics* 2019 16:2 **16**, 164–170 (2019).
- 337 Tschirhart, C. L. *et al.* Imaging orbital ferromagnetism in a moiré Chern insulator. *Science* (1979) **372**,
338 1323–1327 (2021).
- 339 Wollman, D. A., Van Harlingen, D. J., Lee, W. C., Ginsberg, D. M. & Leggett, A. J. Experimental
340 determination of the superconducting pairing state in YBCO from the phase coherence of YBCO-Pb dc
341 SQUIDs. *Phys Rev Lett* **71**, 2134 (1993).

342 Tsuei, C. C. & Kirtley, J. R. Pairing symmetry in cuprate superconductors. *Rev. Mod. Phys.* **72**, 969–1016
343 (2000).

344 Li, Y., Xu, X., Lee, M. H., Chu, M. W. & Chien, C. L. Observation of half-quantum flux in the
345 unconventional superconductor b-Bi₂Pd. *Science* (1979) **366**, 238–241 (2019).

346 Hart, S. *et al.* Induced superconductivity in the quantum spin Hall edge. *Nature Physics* 2014 **10**:9 **10**,
347 638–643 (2014).

348 Wang, W. *et al.* Evidence for an edge supercurrent in the Weyl superconductor MoTe₂. *Science* (1979)
349 **368**, 534–537 (2020).

350 Kasahara, Y. *et al.* Majorana quantization and half-integer thermal quantum Hall effect in a Kitaev spin
351 liquid. *Nature* 2018 **559**:7713 **559**, 227–231 (2018).

352

353 Main Figure Legends

354

355 **Figure 1. Superconductivity in the flat bands of rhombohedral tetralayer graphene Device T3 and**
356 **pentalayer graphene Device P1.** **a**, Illustration of the device structure, in which the tetra- and penta-layer
357 graphene form large twist angle with hBN to avoid the moiré superlattice effect. **b**, The dispersion of
358 conduction band in tetralayer graphene under varying potential difference between top and bottom layer
359 Δ , featuring a flat band bottom enclosing a charge density n_e of $0.6 \times 10^{12} \text{ cm}^{-2}$ per valley per spin at $\Delta = 90$
360 meV. **c&d**, Four-terminal resistance R_{xx} as a function of n_e and gate displacement field D/ϵ_0 taken at zero
361 magnetic field and base temperature (7 mK at the mixing chamber) in tetra- and penta-layer graphene,
362 respectively. Three regions show zero R_{xx} (labeled as 'SC1-3' respectively) and superconductivity. **e&f**,
363 Temperature dependence of the superconducting states in tetra- and penta-layer graphene, respectively.
364 The SC1-3 curves are taken at the labeled $(n, D/\epsilon_0)$ in the units of (10^{12} cm^{-2} , V/nm), respectively.

365

366 **Figure 2. TRSB and valley polarization in the neighboring states in the tetralayer Device T3.** **a&b**, R_{xx}
367 and R_{xy} maps at 0.1 T and base temperature (7 mK at the mixing chamber), extracted by symmetrizing and
368 anti-symmetrizing the data taken at $B_\perp = \pm 0.1$ T. In **b**, SC1 (SC2) is surrounded (neighbored) by states that
369 show anomalous Hall signals. The value of normal Hall signals at the same n_e can be seen in the high- D
370 part of the map. **c**, R_{xy} and R_{xx} during forward (dashed curves) and backward (solid curves) scans of B_\perp at
371 the purple and blue dots in **b**, respectively. The magnetic hysteresis and anomalous Hall signal indicate
372 valley polarization. **d**, R_{xx} map taken at $B_\perp = 1$ T. The period of quantum oscillations indicates a quarter
373 metal (as labeled by 'QM') that neighbors SC1. Together with the data in **c**, this neighboring state to SC1
374 is a spin- and valley-polarized quarter-metal. **e&f**, R_{xx} and R_{xy} as a function of n_e and B_\perp along the dashed
375 line in **a&b** ($D/\epsilon_0 = 1.013$ V/nm), respectively. The phase boundary between the QM and SC1 remains at
376 the same n_e , indicating the orbital magnetization is continuous across the boundary. The left boundary of
377 SC1 (indicated by zero R_{xx} and R_{xy}) even expands in magnetic field, confirming its orbital magnetic nature.

378

379 **Figure 3. Spin and valley polarization in the superconducting states in the pentalayer Device P1.** **a-d**, n_e -
 380 D maps of R_{xx} in SC1 at in-plane magnetic field $B_{\parallel} = 0, 1, 3, 5$ T, respectively (an out-of-plane magnetic
 381 field $B_{\perp} = 0.2$ T is applied to prevent the random fluctuation of R_{xx}). **e-h**, n_e - D maps of R_{xx} in SC2 at in-plane
 382 magnetic field $B_{\parallel} = 0, 1, 3, 4$ T, respectively with an out-of-plane magnetic field $B_{\perp} = 0$. **i&j**, R_{xx} during
 383 forward (dashed curves) and backward (solid curves) scans of B_{\perp} at the ($D/\epsilon_0 = 0.96$ V/nm, $n_e = 0.7 \times 10^{12}$ cm⁻²) and ($D/\epsilon_0 = 1.05$ V/nm, $n_e = 0.85 \times 10^{12}$ cm⁻²) in **a** and **d**, respectively. Clearly hysteresis between two zero-
 385 resistance states can be seen in both cases, indicating a ferromagnet-like behavior of the superconductors.
 386 **k&l**, R_{xx} during forward and backward scans of B_{\perp} at the same states as in **i** and **j**, with $B_{\parallel} = 2$ T and 1 T
 387 applied, respectively. Similar hysteresis as in **i&j** can be seen, although the spin is fixed by the in-plane
 388 magnetic field. **m**, Illustration of the three states during the magnetic hysteresis scans in **i-l**, where state I
 389 and III correspond to uniform valley-polarized domains and zero-resistance states, and state II corresponds
 390 to a domain wall between oppositely valley-polarized domains between the voltage contacts and non-zero-
 391 resistance states. **n&o**, R_{xx} during forward and backward scans of B_{\perp} at the same states as in **i** and **j**, with
 392 $B_{\perp} = 0.15$ T applied. No hysteresis is observed in either case, in stark contrast to **i-l**.

393

394 **Figure 4. Temperature-dependent anomalous Hall effects and phase boundary in the tetralayer Device**
 395 **T3.** **a&b**, Symmetrized R_{xx} and anti-symmetrized R_{xy} map at 0.1 T and 480 mK, above the critical
 396 temperatures of SC1 and SC2. The dashed curves outline the boundary of SC1 and SC2, inside which clear
 397 anomalous Hall signals can be seen in the normal states in **b**. **c&d**, Magnetic field scans of R_{xy} at the square,
 398 star, triangle, diamond and dot positions in **b** at 480 and 7 mK, respectively. Clear hysteresis can be seen
 399 in both the states surrounding SC1, as well as in the SC1 region. Such an anomalous Hall signal indicates
 400 TRSB due to the orbital degree-of-freedom, which is absent in any previously reported superconductors. **e**,
 401 Temperature-dependent R_{xy} hysteresis at the star position. At 277 to 521 mK, non-zero value of R_{xy} at $B =$
 402 0 T and a linear R_{xy} vs B (the normal Hall signal) can be seen. Below 277 mK, these components disappear
 403 due to the superconductivity while clear hysteresis can still be seen. **f**, The same R_{xx} map as in **a**, highlighting
 404 (by the orange dashed curve) the phase boundary between the spin- and valley-polarized quarter-metal
 405 (QM) and an undetermined metal (UM). **g**, Temperature-dependent R_{xx} line-cut at $D/\epsilon_0 = 0.923$ V/nm,
 406 where the QM-UM phase boundary gradually shifts as T is lowered. The SC1 state develops to the right of
 407 the boundary, indicating the QM as the parent state of SC1. **h**, Line-cuts from **g**, showing the QM-UM
 408 phase boundary as a kink in R_{xx} which shifts to lower n_e as T is lowered.

409

410 **Figure 5. Superconductivity close to the BCS-BEC crossover.** **a&b**, Dependence of resistances in SC1-3
 411 on B_{\perp} at 7 mK in the tetralayer Device T3 and pentalayer Device P1, respectively. The curves were taken
 412 at ($n, D/\epsilon_0$) labeled in the figure in the units of (10^{12} cm⁻², V/nm), respectively. **c**, Coherence length ξ_{GL} as a
 413 function of charge density in SC1-3. Here the critical magnetic field and its uncertainties are defined as the
 414 field at 10% and field range between 5% and 15% of the normal state resistance, respectively. The dashed
 415 lines represent the inter-particle distance derived from the corresponding n_e . The ξ_{GL} in SC1 in the
 416 pentalayer device is close to the inter-particle distance, indicating strongly coupled Cooper pairing that is
 417 close to the BEC-BCS crossover but is still mainly on the BCS side.

418

419

420 **Methods**

421 **Device fabrication**

422 The graphene, WSe₂ (from HQ graphene) and hBN flakes were prepared by mechanical exfoliation onto
423 SiO₂/Si substrates. The rhombohedral domains of tetra-layer and penta-layer graphene were identified and
424 confirmed using IR camera⁵⁶, near-field infrared microscopy, and Raman spectroscopy and isolated by
425 cutting with a femtosecond laser. The van der Waals heterostructure was made following a dry transfer
426 procedure. We picked up the top hBN, graphite, middle hBN, WSe₂ and the tetralayer (pentalayer) graphene
427 using polypropylene carbonate film and landed it on a prepared bottom stack consisting of an hBN and
428 graphite bottom gate. We misaligned the long straight edge of the graphene and hBN flakes to avoid forming
429 a large moiré superlattice. The device was then etched into a multiterminal structure using standard e-beam
430 lithography and reactive-ion etching. We deposited Cr–Au for electrical connections to the source, drain
431 and gate electrodes.

432 **Transport measurement**

433 The devices were measured mainly in a Bluefors LD250 dilution refrigerator at MIT with a lowest
434 electronic temperature of around 40 mK. Stanford Research Systems SR830 lock-in amplifiers and SP1004
435 voltage preamplifiers from Basel Precision Instruments were used to measure the longitudinal and Hall
436 resistance R_{xx} and R_{xy} with an AC frequency at 17.77 Hz. The DC and AC currents are generated by Keysight
437 33210A function generator through a 100 MΩ resistor. The AC current excitation was limited to be below
438 0.5 nA. All measurement lines are filtered by the Basel Precision Instruments microwave filter MFT25.
439 Device T1 was also measured in an Oxford dilution refrigerator at Florida State University. Device P1 was
440 also measured at the University of Basel in a Leiden MNK126-700 dilution refrigerator with a base
441 temperature of ~5mK. An MFLI Zurich Instrument lock-in amplifier (at 17.77 Hz) modulated the AC signal
442 on the DC, followed by a 1 MΩ resistor to fix the current. Basel Precision Instruments preamps were used
443 to measure differential currents and voltages. Keithley 2400 source-meters were used to apply top and
444 bottom gate voltages. Top-gate voltage V_t and bottom-gate voltage V_b are swept to adjust doping density
445 $n_e = (C_t V_t + C_b V_b)/e$ and displacement field $D/\varepsilon_0 = (C_t V_t - C_b V_b)/2$, where C_t and C_b are top-gate and bottom-
446 gate capacitance per area calculated from the Landau fan diagram.

447 **Tight-binding model calculation**

448 The single-particle band structure of the rhombohedral stacked tetralayer graphene is calculated from an
449 effective 8-band Slonczewski-Weiss-McClure type tight-binding model

$$450 \quad H = \begin{pmatrix} u/2 & v_0\pi^\dagger & v_4\pi^\dagger & v_3\pi & 0 & \gamma_2/2 & 0 & 0 \\ v_0\pi & u/2 & \gamma_1 & v_4\pi^\dagger & 0 & 0 & 0 & 0 \\ v_4\pi & \gamma_1 & u/6 & v_0\pi^\dagger & v_4\pi^\dagger & v_3\pi & 0 & \gamma_2/2 \\ v_3\pi^\dagger & v_4\pi & v_0\pi & u/6 & \gamma_1 & v_4\pi^\dagger & 0 & 0 \\ 0 & 0 & v_4\pi & \gamma_1 & -u/6 & v_0\pi^\dagger & v_4\pi^\dagger & v_3\pi \\ \gamma_2/2 & 0 & v_3\pi^\dagger & v_4\pi & v_0\pi & -u/6 & \gamma_1 & v_4\pi^\dagger \\ 0 & 0 & 0 & 0 & v_4\pi & \gamma_1 & -u/2 & v_0\pi^\dagger \\ 0 & 0 & \gamma_2/2 & 0 & v_3\pi^\dagger & v_4\pi & v_0\pi & -u/2 \end{pmatrix}$$

451 in the basis of (A1, B1, A2, B2, A3, B3, A4, B4), like the trilayer case^{57,58}. Here $v_i = \sqrt{3}a_0\gamma_i/2\hbar$ and a_0
452 = 0.246 nm. The parameters we used are: $\gamma_0=3.25\text{eV}$, $\gamma_1=0.400\text{ eV}$, $\gamma_2=-0.0166\text{eV}$, $\gamma_3=-0.293\text{ eV}$, $\gamma_4=$
453 0.144 eV. A perpendicular displacement field can introduce a screened potential difference between the top
454 and bottom layers, denoted by Δ . The band structure for rhombohedral pentalayer graphene is calculated
455 using the same parameters using a 10-band model.

456 The estimation of effective mass in this case is complex due to the trigonally-warped non-parabolic
457 band structure. The effective mass is highly dependent on the density and electric field. We define an
458 averaged effective mass by calculating the density and average kinetic energy⁵⁹

$$459 \quad n = \int_{E_m}^{E_F} \frac{d^2k}{(2\pi)^2}, W = \frac{1}{n} \int_{E_m}^{E_F} \frac{d^2k}{(2\pi)^2} (E(\mathbf{k}) - E_m)$$

460 where E_F and E_m denotes the Fermi energy and the conduction band minimum respectively. $E(\mathbf{k})$ is the band
461 energy at momentum \mathbf{k} . Then we compare this to a parabolic band with the same density n and same average
462 kinetic energy W and get the effective mass. We plot the effective mass m^* and Fermi energy E_F as a
463 function of density when $\Delta = 90\text{ meV}$ (Extended Data Fig. 12a) and when $n_e = 0.5 * 10^{12}\text{ cm}^{-2}$ (Extended
464 Data Fig. 12b) near which superconductivity appears. We also plot the effective mass m^* and Fermi energy
465 E_F as a function of density when $\Delta = 63\text{ meV}$ (Extended Data Fig. 12c) and when $n_e = 0.6 * 10^{12}\text{ cm}^{-2}$
466 (Extended Data Fig. 12d) The calculation assumes there is only one single-valley polarized band, suggested
467 by the experiment.

468 Previous experimental efforts on graphene-based two-dimensional material heterostructures

469 Introducing the moiré superlattice between adjacent graphene layers⁶⁰⁻⁶², or between graphene and hBN⁶³,
470 has led to observations of superconducting and correlated insulating states, resembling the phase diagrams
471 of high- T_c superconductors. More recently, it was shown that crystalline graphene with the rhombohedral
472 stacking order could also exhibit superconductivity in the absence of moiré effects⁶⁴⁻⁷². Rhombohedral
473 stacked multilayer graphene hosts gate-tunable flat bands which drastically promotes correlation effects,
474 resulting in diverse ground states characterized by broken spin and/or valley symmetries arising from
475 exchange interactions⁷³⁻⁷⁸. By introducing moiré potential via an adjacent hBN layer and under the
476 application of a perpendicular electric field, multilayer rhombohedral graphene/hBN moiré can host integer

477 and fractional quantum anomalous Hall effects^{56,79,80}, happening roughly in the same (n_e , D) range as the
478 superconducting state SC1 reported in this work where the moiré effect is negligible.

479

480 **Device T1, T2 and P2**

481 Device T2 has a monolayer WSe₂ on top of the tetralayer graphene. Device T1 has a bilayer WSe₂ beneath
482 the tetralayer graphene. Device P2 is a bare pentalayer graphene without WSe₂. Due to the contact
483 geometry, we can reliably measure the superconducting phases only when the electrons in the conduction
484 band are pushed towards the WSe₂ in Device T1, and when electrons in the conduction band are pushed
485 away from WSe₂ in Device T2.

486 The general phase diagram of Device T1 and T2 are similar to that of Device T3. In Device T1,
487 SC1, SC2 and SC3 are observed (Extended Data Fig. 7&8). At $B = 0$ T, both SC1 and SC2 show fluctuations
488 when scanning the gate voltages while SC3 does not. At $B_{\perp} = 0.1$ T, SC3 is destroyed while SC1 and SC2
489 remains. Magnetic field scans reveal anomalous Hall signals surrounding SC1 (Extended Data Fig. 7).
490 There is also magnetic hysteresis inside SC1. SC1 survives up to $B_{\perp} \sim 0.8$ T and the phase boundary between
491 SC1 and the higher-density-quarter-metal (QM) remains unchanged or even slightly leans towards the QM
492 (Extended Data Fig. 8). SC2 survives up to ~ 0.4 T (Extended Data Fig. 8).

493 In Device T2, we observed SC1, SC2 and SC3, as well as an additional SC4 (Extended Data Fig.
494 1). The phase boundary of quarter metal shifts to lower density as the temperature decreases and SC1
495 emerges from the QM. Such behavior was observed in all three devices (Extended Data Fig. 11).

496 Although sharing similar qualitative behaviors, the three devices are quantitatively different. For
497 example, the $T_{\text{BKT}, \text{SC1}}$ for Device T1, T2 and T3 are 160 mK, 210 mK and 300 mK respectively. The
498 difference could originate from the existence of WSe₂ and also the device quality variations.

499 The general phase diagram and behaviors of Device P1 (Extended Data Fig. 9) and P2 (Extended
500 Data Fig. 10) are similar.

501 **Fluctuations in resistance maps and time domain**

502 When measuring R_{xx} maps at close to zero magnetic field, we often observe fluctuations in the SC1, SC2
503 and the neighboring QM states. This is a universal observation (see Fig. 1 for T3, Extended Data Fig. 1 for
504 T2, Extended Data Fig. 7 for T1). The frequency of such fluctuations, however, depends on the details of
505 the specific device and measurement, such as the coercive magnetic field (less when the coercive field is
506 bigger) and the cooling history (less when field-cooled). When fixing the n_e and D , it is also possible to see
507 fluctuations of R_{xx} as a function of time, such as shown in Extended Data Fig. 1j. The fluctuations in the
508 QM state we observed has also been observed in previous experiments in rhombohedral trilayer graphene,
509 and was attributed to flipping of the valley-polarization and orbital magnetism⁶⁴. The fluctuations we
510 observed in the SC1 and SC2 states, however, have not been reported in any superconductors. We think the

511 origin of these fluctuations in the superconducting states is also the flipping of valley-polarization and
512 orbital magnetism.

513 **Quantum oscillations and fermiology of the neighboring states of SC1 and SC2**

514 While the spin- and valley-polarized quarter metal are clearly established by the quantum oscillation data
515 and the valley-orbital-magnetic hysteresis, the Fermi surface topology in the UM state in Fig. 4f is much
516 less clear. This can be seen from Fig. 2 and Extended Data Fig. 9, where no clear quantum oscillations can
517 be observed in the region to the lower density side of the QM-UM phase boundary.

518 Extended Data Fig. 6b&c show the Landau fan at $D/\varepsilon_0 = 1.123$ V/nm and the corresponding FFT
519 spectra. Quantum oscillations can be seen starting at ~ 1.5 T in the former panel, and a diagonal feature can
520 be seen in the latter panel. The diagonal feature is similar to that observed in the annular Fermi-surfaced
521 metal state in rhombohedral tri-layer graphene⁷³, which has a frequency above 1. The corresponding low-
522 frequency feature observed in tri-layer graphene, however, is missing from our data. Admittedly, the low-
523 frequency component of FFT is usually more difficult to extract. This is especially true in our case, due to
524 the large effective mass in the flat conduction band. Based on these observations, we can only speculate the
525 UM state to be possibly a spin- and valley-polarized quarter-metal with an annular Fermi surface. This
526 undetermined nature of the UM state (which is to the lower-density-side of the QM-UM phase boundary),
527 however, does not affect visualizing the temperature dependence of phase evolutions and our conclusion of
528 SC1 stemming from a spin- and valley-polarized QM parent state.

529 **Extraction of coherence length**

530 We define the critical magnetic field $B_{\perp,c}$ as the field when the R_{xx} reaches 10% of the normal state resistance
531 and its uncertainty as the field range between 5% and 15% (see Extended Data Fig. 9), and extract the

532 phenomenological Ginzburg-Landau superconducting coherence length as $\xi_{GL} = \left(\frac{\Phi_0}{2\pi B_{\perp,c}} \right)^{\frac{1}{2}}$, where $\Phi_0 = \frac{\hbar}{2e}$
533 is the superconducting magnetic flux quantum. We note that our coherence length is extracted directly from
534 the critical magnetic field, instead of using the Ginzburg–Landau relation $T_c/T_{c0} = 1 - (2\pi\xi_{GL}^2/\Phi_0)B_{\perp}$
535 (where T_{c0} is the mean-field critical temperature at zero magnetic field) and performing a linear fitting near
536 T_c . An analysis of SC1 based on the latter approach will result in an even shorter coherence length and even
537 stronger coupling strength.

538

539 **Data availability** The data shown in the figures are available from <https://doi.org/10.7910/DVN/IADV2O>.
540 Other data that support the finding of this study are available from the corresponding authors upon request.

541

542 **Methods only references**

543

- 544 Lu, Z. *et al.* Extended Quantum Anomalous Hall States in Graphene/hBN Moiré Superlattices. *arXiv*:
545 2408.10203 (2024).
- 546 Zhang, F., Sahu, B., Min, H. & MacDonald, A. H. Band structure of ABC-stacked graphene trilayers. *Phys.*
547 *Rev. B* **82**, 035409 (2010).
- 548 Yang, J. *et al.* Spectroscopy signatures of electron correlations in a trilayer graphene/hBN moiré
549 superlattice. *Science* (1979) **375**, 1295–1299 (2022).
- 550 Seiler, A. M. *et al.* Quantum cascade of correlated phases in trigonally warped bilayer graphene. *Nature*
551 2022 **608**:7922 **608**, 298–302 (2022).
- 552 Cao, Y. *et al.* Unconventional superconductivity in magic-angle graphene superlattices. *Nature* 2018
553 **556**:7699 **556**, 43–50 (2018).
- 554 Yankowitz, M. *et al.* Tuning superconductivity in twisted bilayer graphene. *Science* (1979) **363**, 1059–
555 1064 (2019).
- 556 Lu, X. *et al.* Superconductors, orbital magnets and correlated states in magic-angle bilayer graphene.
557 *Nature* **574**, 653–657 (2019).
- 558 Chen, G. *et al.* Signatures of tunable superconductivity in a trilayer graphene moiré superlattice. *Nature*
559 **572**, 215–219 (2019).
- 560 Zhou, H., Xie, T., Taniguchi, T., Watanabe, K. & Young, A. F. Superconductivity in rhombohedral trilayer
561 graphene. *Nature* 2021 **598**:7881 **598**, 434–438 (2021).
- 562 Pantaleón, P. A. *et al.* Superconductivity and correlated phases in non-twisted bilayer and trilayer
563 graphene. *Nature Reviews Physics* 2023 **5**:5 **5**, 304–315 (2023).
- 564 Zhang, Y. *et al.* Enhanced superconductivity in spin-orbit proximitized bilayer graphene. *Nature* 2023
565 **613**:7943 **613**, 268–273 (2023).
- 566 Holleis, L. *et al.* Ising Superconductivity and Nematicity in Bernal Bilayer Graphene with Strong Spin Orbit
567 Coupling. *arXiv*:2303.00742 (2023).
- 568 Li, C. *et al.* Tunable superconductivity in electron- and hole-doped Bernal bilayer graphene. *Nature* 2024
569 **631**:8020 **631**, 300–306 (2024).
- 570 Zhang, Y. *et al.* Twist-Programmable Superconductivity in Spin-Orbit Coupled Bilayer Graphene. *arXiv*:
571 2408.10335 (2024).
- 572 Patterson, C. L. *et al.* Superconductivity and spin canting in spin-orbit proximitized rhombohedral trilayer
573 graphene. *arXiv*: 2408.10190 (2024).
- 574 Yang, J. *et al.* Diverse Impacts of Spin-Orbit Coupling on Superconductivity in Rhombohedral Graphene.
575 *arXiv*: 2408.09906 (2024).
- 576 Zhou, H. *et al.* Isospin magnetism and spin-polarized superconductivity in Bernal bilayer graphene.
577 *Science* (1979) **375**, 774–778 (2022).

- 578 Zhou, H. *et al.* Half- and quarter-metals in rhombohedral trilayer graphene. *Nature* 2021 **598**:7881 **598**,
579 429–433 (2021).
- 580 Han, T. *et al.* Orbital Multiferroicity in Pentalayer Rhombohedral Graphene. *Nature* **623**, 41–47 (2023).
- 581 Han, T. *et al.* Correlated Insulator and Chern Insulators in Pentalayer Rhombohedral Stacked Graphene.
582 *Nat. Nanotechnology* **19**, 181–187 (2024).
- 583 Liu, K. *et al.* Spontaneous broken-symmetry insulator and metals in tetralayer rhombohedral graphene.
584 *Nat Nanotechnol* **19**, 188–195 (2024).
- 585 Sha, Y. *et al.* Observation of a Chern insulator in crystalline ABCA-tetralayer graphene with spin-orbit
586 coupling. *Science* (1979) **384**, 414–419 (2024).
- 587 Han, T. *et al.* Large quantum anomalous Hall effect in spin-orbit proximitized rhombohedral graphene.
588 *Science* **384**, 647–651 (2024).
- 589 Lu, Z. *et al.* Fractional quantum anomalous Hall effect in multilayer graphene. *Nature* 2024 **626**:8000
590 **626**, 759–764 (2024).
- 591 Xie, J. *et al.* Even- and Odd-denominator Fractional Quantum Anomalous Hall Effect in Graphene Moire
592 Superlattices. *arXiv*: 2405.16944 (2024).

593

594 **Acknowledgement**

595 We acknowledge the helpful discussions with S.D. Sarma, J. Sau, X.G. Wen, S. Todadri, F. Zhang, A.
596 Vishwanath, P. Lee, B. Ramshaw, E.A. Kim, A. MacDonald, T. Devakul and A. Young. This study was
597 supported by the US Department of Energy, Office of Science, Basic Energy Sciences, Materials Sciences
598 and Engineering Division under grant no. DE-SC0025325. Device fabrication was performed at the Harvard
599 Center for Nanoscale Systems and MIT.nano. T.H. acknowledges support from a Mathworks Fellowship.
600 L.F. was supported by a Simons Investigator Award from the Simons Foundation. Work in Basel was
601 supported by the EU's H2020 MSCA cofund Quantum Science and Technologies at the European Campus
602 (QUSTEC) Grant Nr. 847471, the Swiss National Science Foundation (Grant No. 215757), the Georg H.
603 Endress Foundation, and WSS Research Center for Molecular Quantum Systems (molQ) of the Werner
604 Siemens Foundation. K.W. and T.T. acknowledge support from the JSPS KAKENHI (grant nos. 20H00354,
605 21H05233 and 23H02052) and the World Premier International Research Center Initiative, MEXT, Japan.

606 **Author Contributions**

607 L.J. supervised the project. T.H. and Z.L. performed the DC magneto-transport measurement. Z.H., A.C.,
608 O.S., H.W. and D.M.Z. performed some of the in-plane field measurements (Basel). T.H., L.S., Z.W., W.X.,
609 Y.Y. and S.Y. fabricated the devices. J.Y., J.S., Z.L. and T.H. helped with installing and testing the dilution
610 refrigerator. T.H. and M.Z. performed the band structure calculation. H.L., G.S., Z.H. and P.X. helped with
611 part of measurements on Device T1. K.W. and T.T. grew hBN crystals. L.F. contributed to data analysis.
612 All authors discussed the results and wrote the paper.

613 **Competing Interests** D.M.Z. is a co-founder of Basel Precision Instruments. The other authors declare no
614 competing interests.

615

616 **Extended Data Figures**

617 **Extended Data Figure 1. Superconductivity in rhombohedral tetra-layer graphene Device T2.** **a**, Optical
618 micrograph (Scale bar: $3\mu\text{m}$) and illustration of the structure of rhombohedral tetra-layer graphene,
619 where the electrons are polarized to the layer far away from WSe₂. **b**, Four-terminal resistance R_{xx} as a
620 function of n_e and gate displacement field D/ϵ_0 . Four regions show zero R_{xx} (labeled as 'SC1-4' respectively)
621 and superconductivity. SC1 and SC2 regions show fluctuations while SC3 and SC4 are smooth. **c**,
622 Temperature dependence of the four superconducting states, with critical temperatures extracted from the
623 comparison of I-V with the BKT model. See Extended Data Fig. 2. **d**, Differential resistance dV_{xx}/dI as a
624 function of current I and out-of-plane magnetic field B_\perp in the SC3 and SC4 states, respectively. Both states
625 show peaks of dV/dI as a signature of superconductivity at small magnetic fields. The superconductivity is
626 killed below 30 mT, similar to that of most graphene-based superconductors. **e&f**, R_{xx} and R_{xy} maps at 0.1
627 T, extracted by symmetrizing and anti-symmetrizing the data taken at $B_\perp = \pm 0.1$ T. The fluctuations in SC1,
628 SC2 and neighboring states all disappear. In **f**, SC1 (SC2) is surrounded (neighbored) by states that show
629 anomalous Hall signals. The value of normal Hall signals at the same n_e can be seen in the high-D part of
630 the map. **g&h**, Magnetic hysteresis scans of R_{xy} taken at the red and orange circle positions in **d**, showing
631 loops that are consistent with the anomalous Hall signals in **f**. **i**, R_{xx} map taken at $B_\perp = 1.5$ T. The period
632 of quantum oscillations indicates a quarter-metal (as labeled by the arrow and 'QM') that neighbors SC1.
633 Combined with the anomalous Hall signals as shown in **f**, this QM is a spin- and valley-polarized phase. **j**,
634 R_{xx} in SC1 (at $n_e = 0.55*10^{12} \text{ cm}^{-2}$ and $D/\epsilon_0 = 1.02 \text{ V/nm}$) as a function of time, featuring fluctuations when
635 gate voltages are fixed. **k&l**, Representative magnetic hysteresis of R_{xx} taken in SC1 (at $n_e = 0.57*10^{12} \text{ cm}^{-2}$
636 and $D/\epsilon_0 = 1.05 \text{ V/nm}$) and SC2 (at $n_e = 0.7*10^{12} \text{ cm}^{-2}$ and $D/\epsilon_0 = 1.16 \text{ V/nm}$). We note that one of the
637 four terminals was damaged during measurement, resulting in only three-terminal resistance measurement
638 possible.

639

640 **Extended Data Figure 2. Detailed characterizations of SC1-4 in Device T2.** **a&b**, Differential resistance
641 dV_{xx}/dI vs I and B_\perp for SC1 and SC2 in Device T2, respectively. The vanishing differential resistance persists
642 to ~ 1 T and ~ 0.6 T in SC1 and SC2, respectively. **c**, B - n_e map at $D/\epsilon_0 = 1.14 \text{ V/nm}$. **d-g**, Temperature
643 dependence of longitudinal and differential resistances and BKT fitting for SC1-4. These are taken at
644 representative (n_e , D) combinations corresponding to Extended Data Fig. 1c. Panels in the same column
645 correspond to a specific superconducting state. Zero resistance, differential resistance peak at critical
646 current, and the BKT scaling ($V_{xx} \propto I^3$, as indicated by the dashed lines in lower panels) can be seen for
647 all of the four superconducting states.

648

649 **Extended Data Figure 3. Anomalous Hall effects and TRSB in the normal state of SC1 and SC2 in**
650 **Device T2.** **a&b**, Symmetrized R_{xx} and anti-symmetrized R_{xy} map at 0.1 T and 450 mK, above the critical
651 temperatures of SC1 and SC2. The dashed curves in **b** outline the boundary of SC1 and SC2, inside which
652 clear anomalous Hall signals can be seen in the normal states. **c&d**, Magnetic hysteresis scans at the dot

653 and triangle positions in **b**. Clear hysteresis loops can be seen in both the states surrounding SC1, as well
654 as in SC1 and SC2. **e&f**, Temperature-dependent anti-symmetrized R_{xy} hysteresis at a state in SC1 and SC2,
655 respectively. Curves are shifted vertically for clarity.

656

657 **Extended Data Figure 4. Superconductivities in Device T3.** **a**, Optical micrograph of the device. Scale
658 bar: $3\mu\text{m}$. **b**, Temperature-dependent differential resistance dV_{xx}/dI versus I at a typical (n_e , D) inside the
659 SC1 region, featuring zero resistance at low current and a pair of peaks at critical current. **c**, Temperature-
660 dependent R_{xx} at a constant D , featuring a density range of zero resistance that corresponds to SC1. **d-f**,
661 Differential resistance at typical n_e - D positions inside SC1 and SC3. The vanishing differential resistance
662 persists to ~ 1 T for SC1, while that of SC3 persists to only ~ 50 mT. **g**, R_{xx} as a function of n_e and B_\perp at
663 $D/\epsilon_0 = 1.113$ V/nm in SC3. The density range corresponding to SC3 keeps shrinking upon B_\perp . **h**, Differential
664 resistance measurement in SC1, showing the superconducting diode effect. **i**, Representative magnetic
665 hysteresis of R_{xx} taken in SC1 (at $n_e = 0.5 \times 10^{12} \text{ cm}^{-2}$ and $D/\epsilon_0 = 0.985$ V/nm).

666

667 **Extended Data Figure 5. Magnetic hysteresis, coercive field and superconducting critical temperature**
668 **in SC1 in Device T3.** **a**, R_{xx} as a function of the out-of-plane magnetic field at different n_e and $D/\epsilon_0 = 0.985$
669 V/nm. The curves are shifted vertically for clarity. The dashed horizontal lines indicate the shift of each
670 curve (which corresponds to zero resistance). Orange and blue arrows indicate the coercive fields, which
671 is defined as the closest-to-zero magnetic field where R_{xx} rises rapidly. **b**, Color map of R_{xx} versus T and n_e .
672 **c**, Summary of the coercive fields and the superconducting T_c at different n_e and $D/\epsilon_0 = 0.985$ V/nm. **d-f**,
673 same as **a-c** but for $D/\epsilon_0 = 1.015$ V/nm.

674

675 **Extended Data Figure 6. Magnetic hysteresis, quantum oscillations and temperature-dependence of SC1**
676 **in Device T3.** **a**, The n_e - D map of R_{xx} taken at zero magnetic field in Device T3. **b**, Landau fan diagram
677 taken at $D/\epsilon_0 = 1.123$ V/nm, revealing quantum oscillations starting at $B_\perp \sim 1.5$ T. **c**, Fast Fourier-transform
678 spectra of data in **b**. A diagonal feature above $f_v = 1$ suggests a quarter-metal state with annular Fermi
679 surface. However, the low-frequency component of this annular Fermi-surfaced metal is not clear from the
680 data. **d**, Out-of-plane magnetic field scans of R_{xx} at different (n_e , D) indicated by the colored dots in **a**.
681 Magnetic hysteresis was observed across a large range of (n_e , D) parameter space across SC1. **e-g**, Upper
682 panels: R_{xx} as a function of T and n_e at three displacement fields cutting through SC1. In all cases, there is
683 a clear boundary as pointed out by the black arrow at above T_c . This boundary shifts to lower n_e values as
684 the temperature is lowered. Superconductivity domes emerge within the phase to the right of this boundary,
685 suggesting this phase to the right (the spin- and valley-polarized quarter-metal) is the parent state of SC1.
686 Lower panels: line-cuts at $T = 400$ mK from the upper panels, featuring kinks that corresponds to the phase
687 boundary between the spin- and valley-polarized quarter-metal and the metal state at lower densities.

688

689 **Extended Data Figure 7. Superconductivities in Device T1.** **a**, Optical micrograph (Scale bar: $3\mu\text{m}$) and
690 device configuration, where electrons are polarized to the bottom layer of tetra-layer graphene with WSe2
691 at proximity. **b&c**, The n_e - D maps of R_{xx} at $B_\perp = 0$ T and base temperature, corresponding to opposite
692 sweeping directions of n_e , respectively. Three superconducting regions labeled as SC1-3 similar to in

693 Device T2 and T3 can be seen. Some fluctuations can be seen in SC1, SC2 and the neighboring metallic
694 region. **d**, The n_e -D map of R_{xx} at $B_\perp = 1.5$ T and base temperature, featuring the quantum oscillations of a
695 quarter-metal to the right of the SC1 region. **e&f**, The n_e -D map of R_{xx} and R_{xy} at $B_\perp = 0.1$ T and base
696 temperature. The fluctuations and SC3 are both suppressed, similar to those observed in Device T2. **g-j**,
697 Magnetic hysteresis scans of R_{xy} taken at the dot, triangle diamond and star positions in **f**, showing
698 jumps/loops that are consistent with the anomalous Hall signals in **f**. **k&l**, Representative magnetic
699 hysteresis of R_{xx} taken in SC1 (at $n_e = 0.54 \times 10^{12} \text{ cm}^{-2}$ and $D/\epsilon_0 = 1.03 \text{ V/nm}$) and SC2 (at $n_e = 0.72 \times 10^{12}$
700 cm^{-2} and $D/\epsilon_0 = 1.17 \text{ V/nm}$).

701

702 **Extended Data Figure 8. Temperature and magnetic field dependence of superconductivity in Device**
703 **T1.** **a-c**, Temperature dependence of R_{xx} , the difference resistance dV_{xx}/dI vs I , and the BKT fitting of SC1
704 respectively. **d**, Temperature-dependent anti-symmetrized R_{xy} hysteresis at a state in SC1. **e-g**, The
705 temperature dependence of R_{xx} , the difference resistance dV/dI vs I , and the BKT fitting of SC2. **h**,
706 Temperature-dependent anti-symmetrized R_{xy} hysteresis at a state in SC2. **i&j**, R_{xx} and R_{xy} as a function of
707 n_e and B_\perp at $D/\epsilon_0 = 1.075 \text{ V/nm}$ (corresponding to SC1), respectively. The phase boundary between the
708 quarter-metal and SC1 remains at the same n_e , indicating the orbital magnetism is continuous across the
709 boundary and SC1 is orbital magnetic. **k&l**, R_{xx} and R_{xy} as a function of n_e and B_\perp at $D/\epsilon_0 = 1.03 \text{ V/nm}$
710 (corresponding to SC1), respectively. The phase boundary between the quarter-metal and SC1 remains at
711 the same n_e , while the left boundary of SC1 even moves against the neighboring state in magnetic field,
712 confirming the orbital magnetic nature of SC1. **m&n**, R_{xx} and R_{xy} as a function of n_e and B_\perp at $D/\epsilon_0 = 1.17$
713 V/nm (corresponding to SC2), respectively. The phase boundaries between SC2 and neighboring states
714 move towards SC2 under magnetic field.

715

716 **Extended Data Figure 9. Superconductivities in Device P1.** **a**, Optical micrograph of the device. Scale
717 bar: 3 μm . **b**, The n_e -D map of R_{xx} at $B_\perp = 1.5$ T and base temperature, featuring the quantum oscillations
718 corresponding to the quarter-metal state neighboring SC1. **c&d**, The n_e -D map of R_{xx} and R_{xy} at $B_\perp = 0.1$
719 T and base temperature, respectively. **e&f**, Magnetic hysteresis of R_{xy} at the green triangle and square
720 positions in **d**. **g&h**, Temperature-dependence of anti-symmetrized R_{xy} in SC1 (corresponding to the red dot
721 position in **d**) and SC2 (corresponding to the blue dot position in **d**), respectively. Curves are shifted
722 vertically for clarity. **h&i**, R_{xx} and R_{xy} as a function of n_e and B_\perp at $D/\epsilon_0 = 0.955 \text{ V/nm}$, respectively. The
723 phase boundary between the quarter-metal and SC1 shifts to slightly higher density, suggesting the orbital
724 magnetic nature of SC1. **j**, The n_e -B map of R_{xx} at $D/\epsilon_0 = 1.05 \text{ V/nm}$, cutting through SC2. **k**, Magnetic field-
725 dependence of R_{xx} in two representative states inside SC1. We use 10% (indicated by the blue dots) of the
726 normal state resistance to extract the T_c , and 5% (red dots) and 15% (green dots) of the normal state
727 resistance to extract the uncertainty of T_c in Figure 5 of the main text. **l**, dV_{xx}/dI versus I in SC1 and SC2 at
728 $(0.61 \times 10^{12} \text{ cm}^{-2}, 0.94 \text{ V/nm})$ and $(0.85 \times 10^{12} \text{ cm}^{-2}, 1.05 \text{ V/nm})$ respectively, featuring zero-resistance at small
729 current and the resistance spikes at critical current. **m**, The n_e -D map of R_{xx} , highlighting (by the orange
730 dashed curve) the phase boundary between the spin- and valley-polarized quarter-metal (QM) and an
731 undetermined metal (UM). **n**, Temperature-dependent R_{xx} line-cut at $D/\epsilon_0 = 0.92 \text{ V/nm}$, where the QM-UM
732 phase boundary (indicated by orange dashed arrow) gradually shifts as T is lowered. The SC1 state
733 develops to the right of the boundary, indicating the QM as the parent state of SC1. **o**, Line-cuts from **n**,

734 showing the QM-UM phase boundary as a kink (orange arrow) in R_{xx} which shifts to lower n_e as T is
735 lowered.

736

737 **Extended Data Figure 10. Superconductivities in Device P2.** **a**, Optical micrograph (scale bar: 3 μm) and
738 illustration of the device configuration. **b**, Magnetic hysteresis in SC1 (at $n_e = 0.61*10^{12} \text{ cm}^{-2}$ and $D/\epsilon_0 =$
739 0.95 V/nm) and SC2 (at $n_e = 0.87*10^{12} \text{ cm}^{-2}$ and $D/\epsilon_0 = 1.07 \text{ V/nm}$) at base temperature, respectively. **c**,
740 The n_e - D map of R_{xx} at zero magnetic field, featuring SC1-SC3. **d**, The n_e - D map of R_{xx} at $B_\perp = 1.5 \text{ T}$,
741 featuring the quarter-metal state to the higher density side of SC1. **e&f**, The n_e - D map of R_{xx} and R_{xy} at B_\perp
742 = 0.1 T and base temperature. **g**, Temperature-dependent magnetic hysteresis of R_{xy} at the 'star' position
743 in **e**. Curves are shifted vertically for clarity. **h&i**, R_{xx} and R_{xy} as a function of n_e and B_\perp along the dashed
744 line in **e**, respectively. The phase boundary between the quarter-metal and SC1 shifts to slightly higher
745 density, suggesting the orbital magnetic nature of SC1.

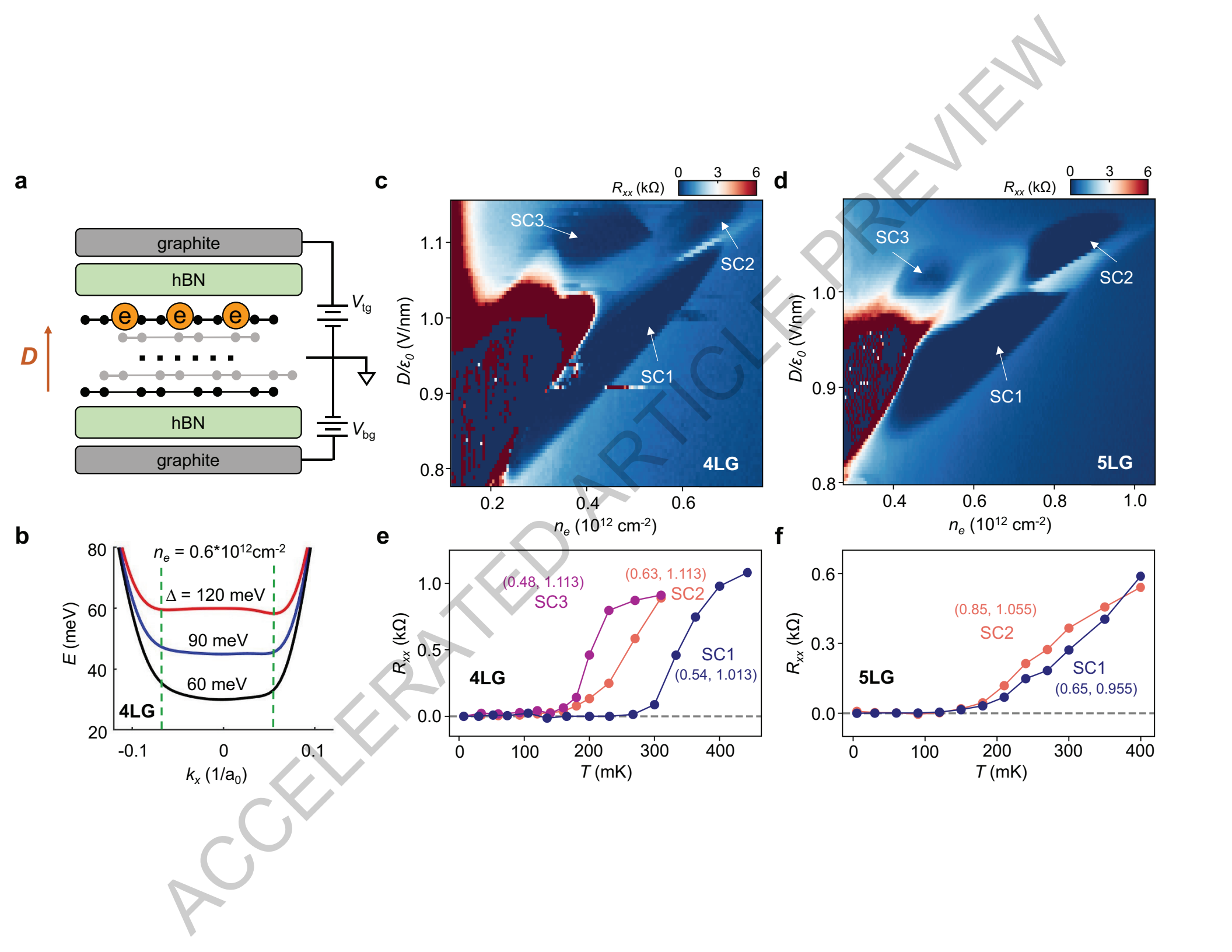
746

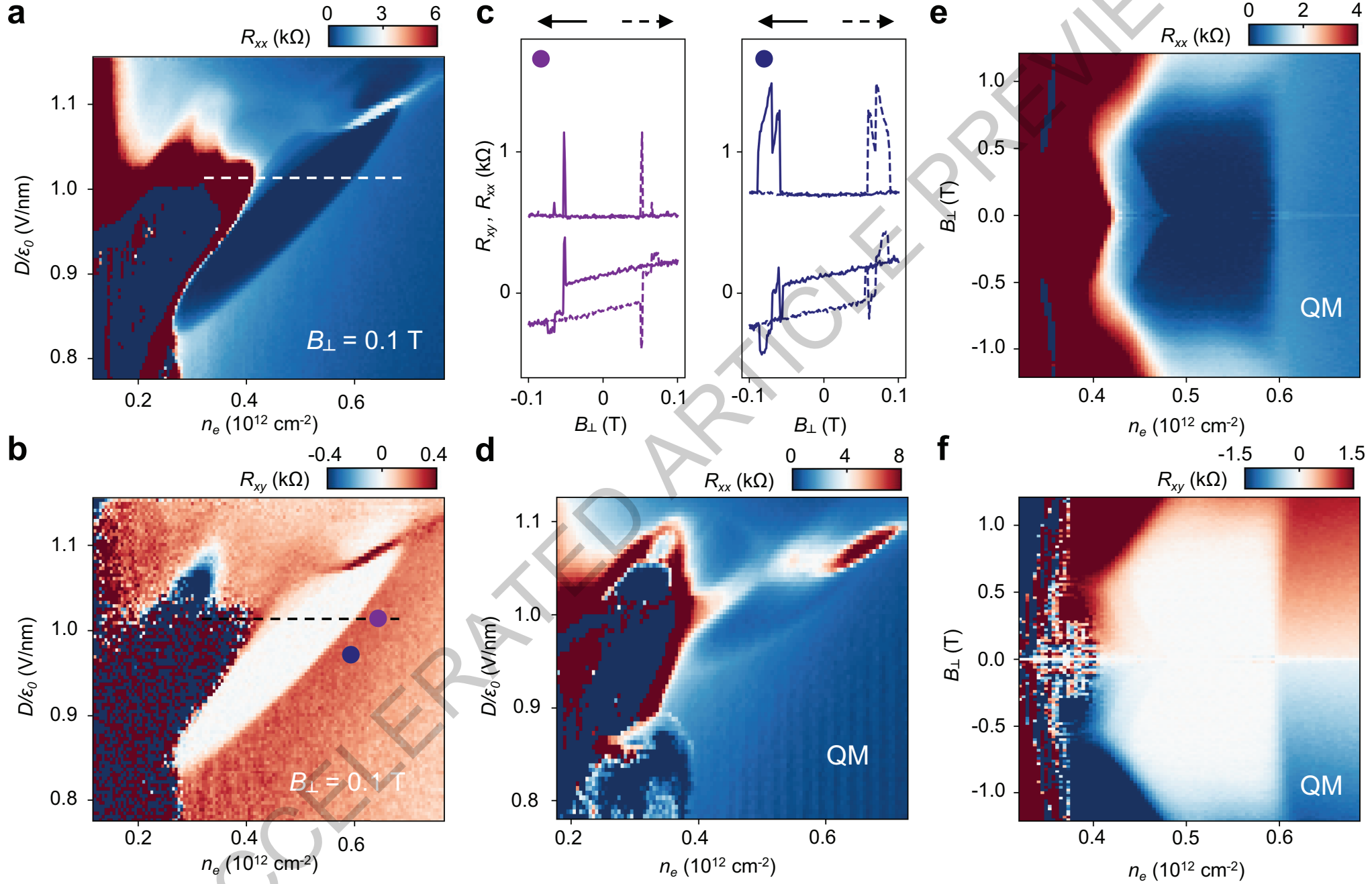
747 **Extended Data Figure 11. Comparison between the highest superconducting transition temperatures of**
748 **SCI in Device T1-T3 and P1.** **a-d**, Upper panels: R_{xx} as a function of temperature and charge density at a
749 constant D that corresponds to highest T_c , in four devices respectively. Lower panels: the same plots as in
750 upper panels with a small unified color scale for a fair comparison. The BKT fitting reveals an increase of
751 T_{BKT} from Device T1 to T3, corresponding to a weakening of spin-orbit-coupling effect.

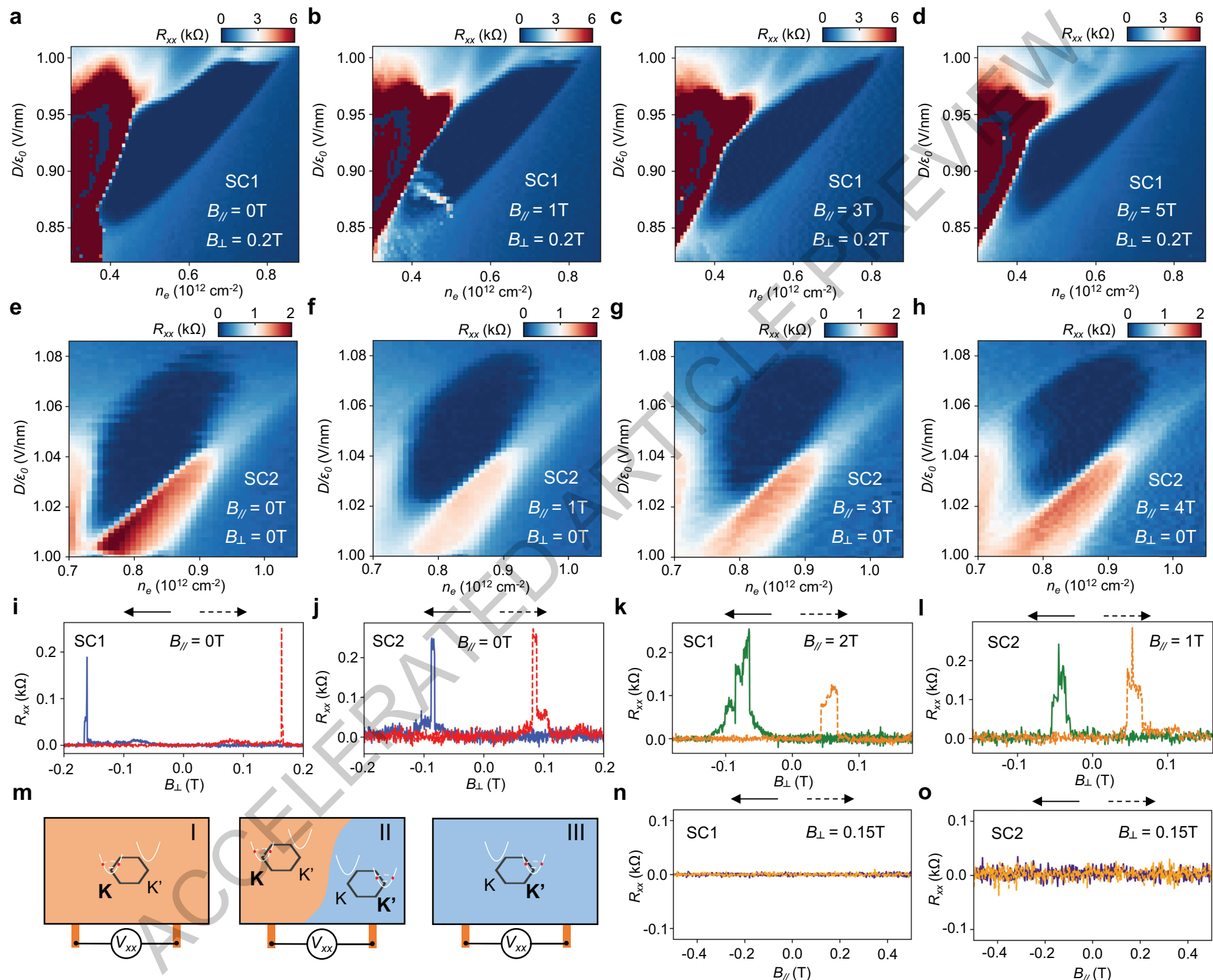
752

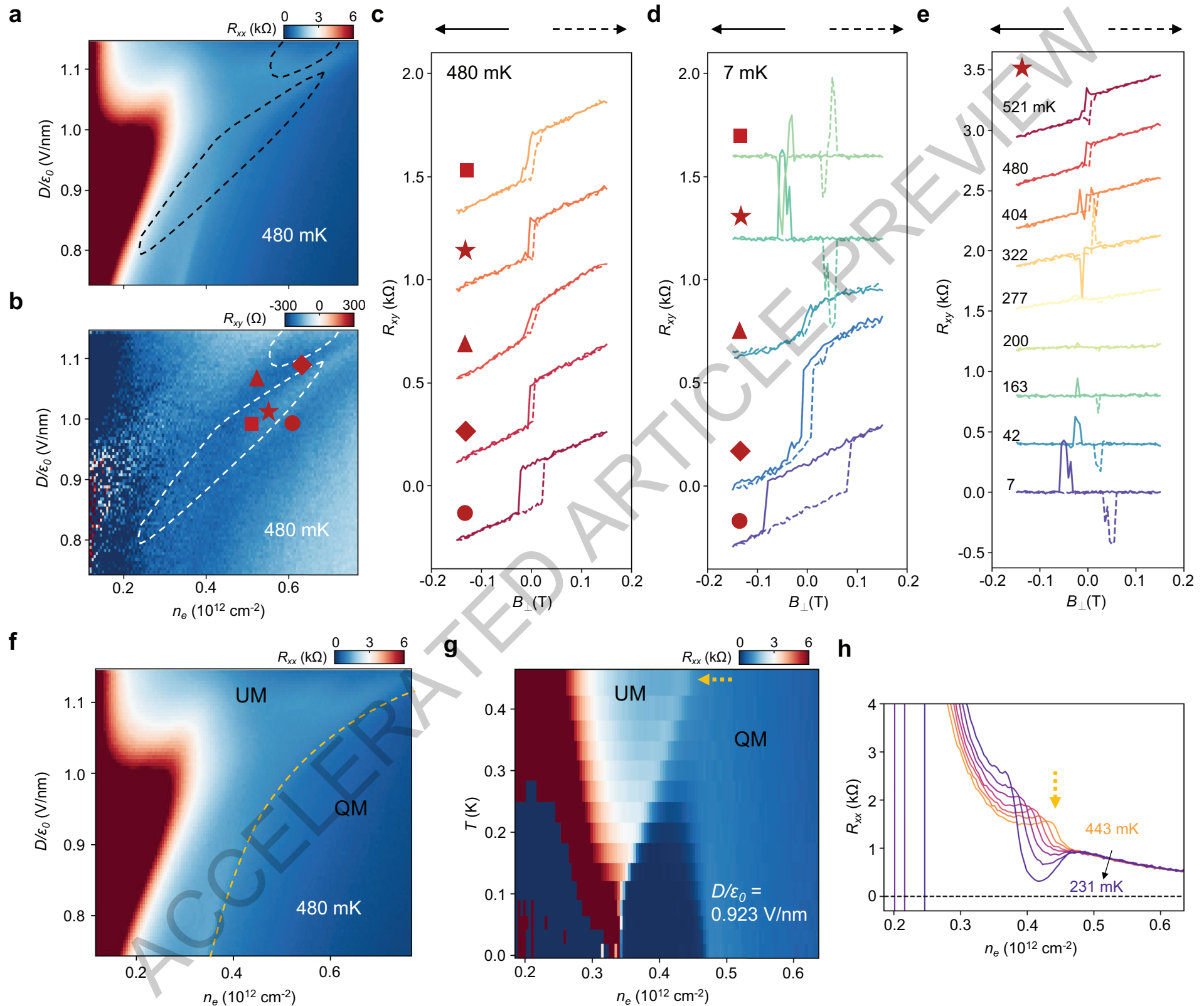
753 **Extended Data Figure 12. Calculation of the effective mass and Fermi energy in tetra- and penta-layer**
754 **rhombohedral graphene.** **a**, Calculation at a fixed potential difference between the top-most and bottom-
755 most layers $\Delta = 90 \text{ meV}$ in tetralayer graphene. **b**, Calculation at a fixed charge density $n_e = 0.5*10^{12} \text{ cm}^{-2}$
756 in tetralayer graphene. **c**, Calculation at a fixed potential difference $\Delta = 110 \text{ meV}$ in pentalayer
757 graphene. **d**, Calculation at a fixed charge density $n_e = 0.6*10^{12} \text{ cm}^{-2}$ in pentalayer.

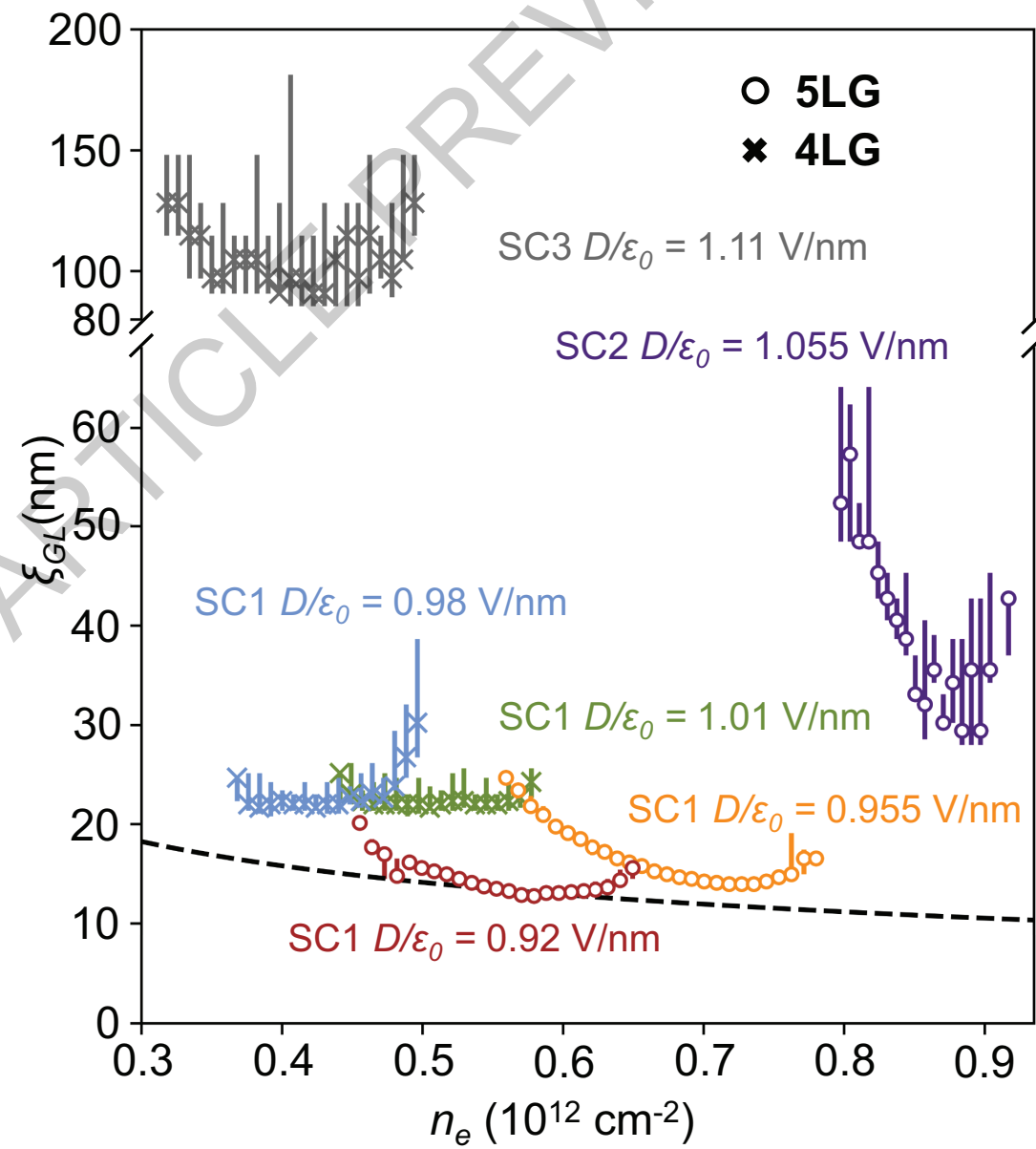
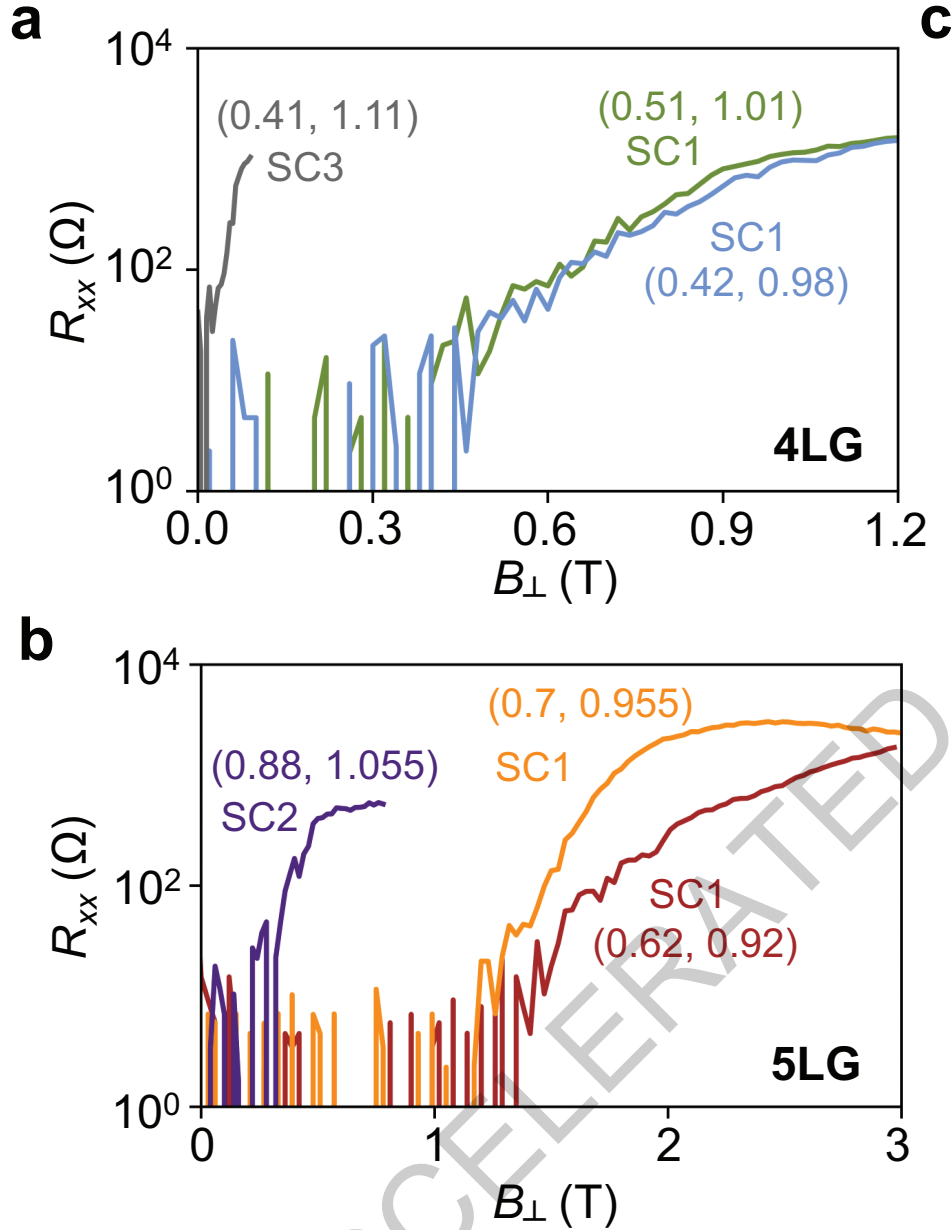
758

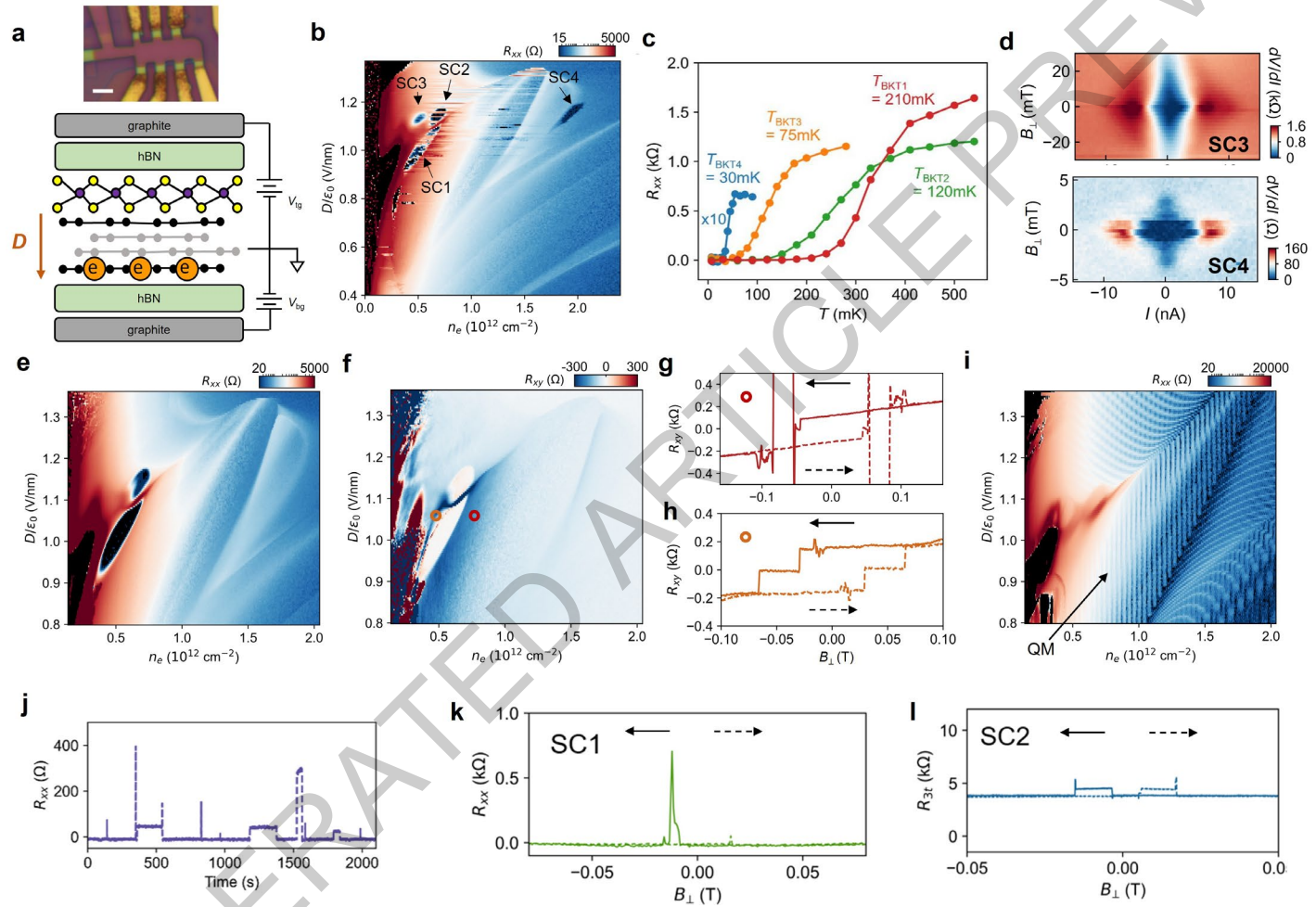




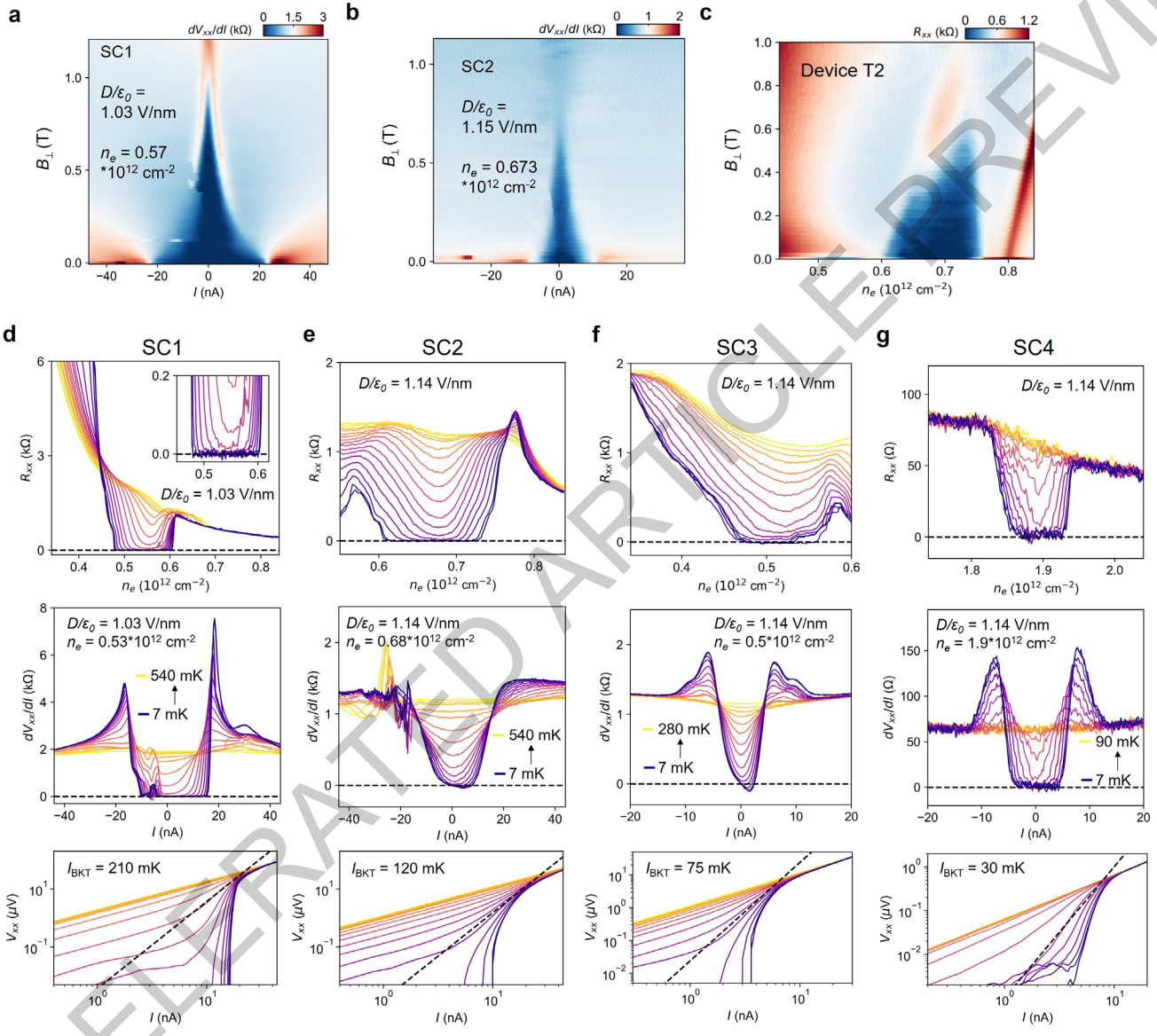




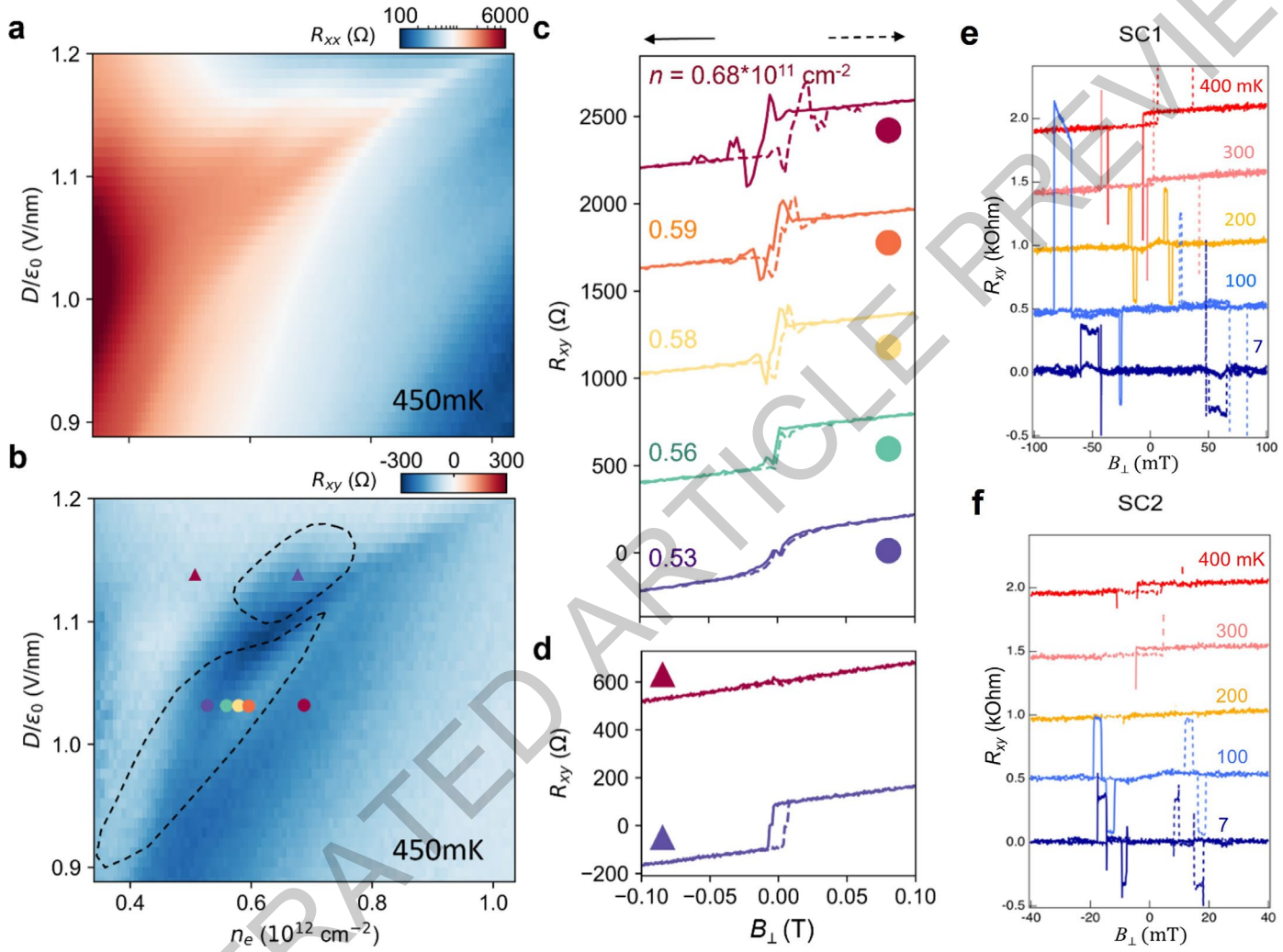




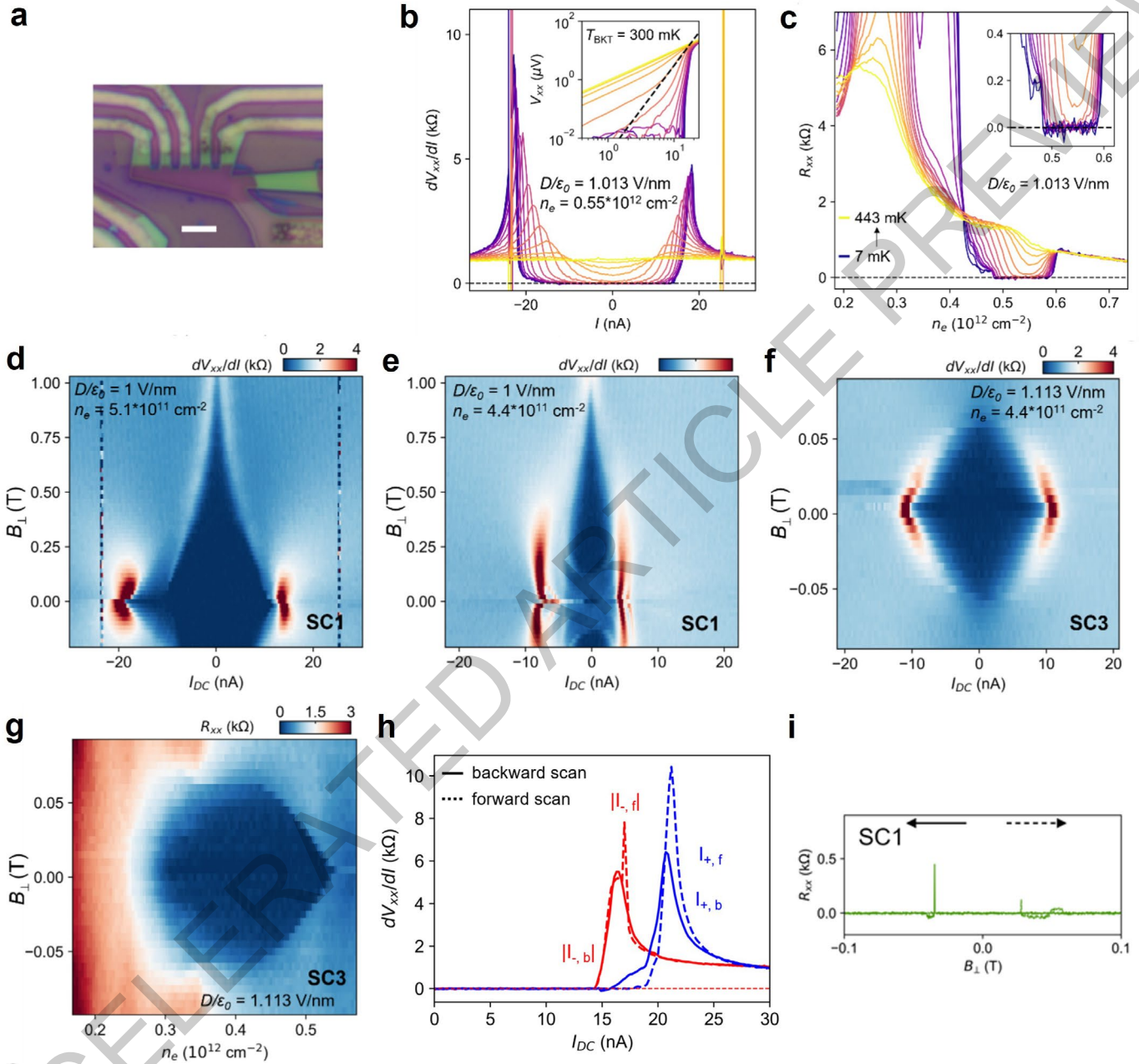
Extended Data Fig. 1



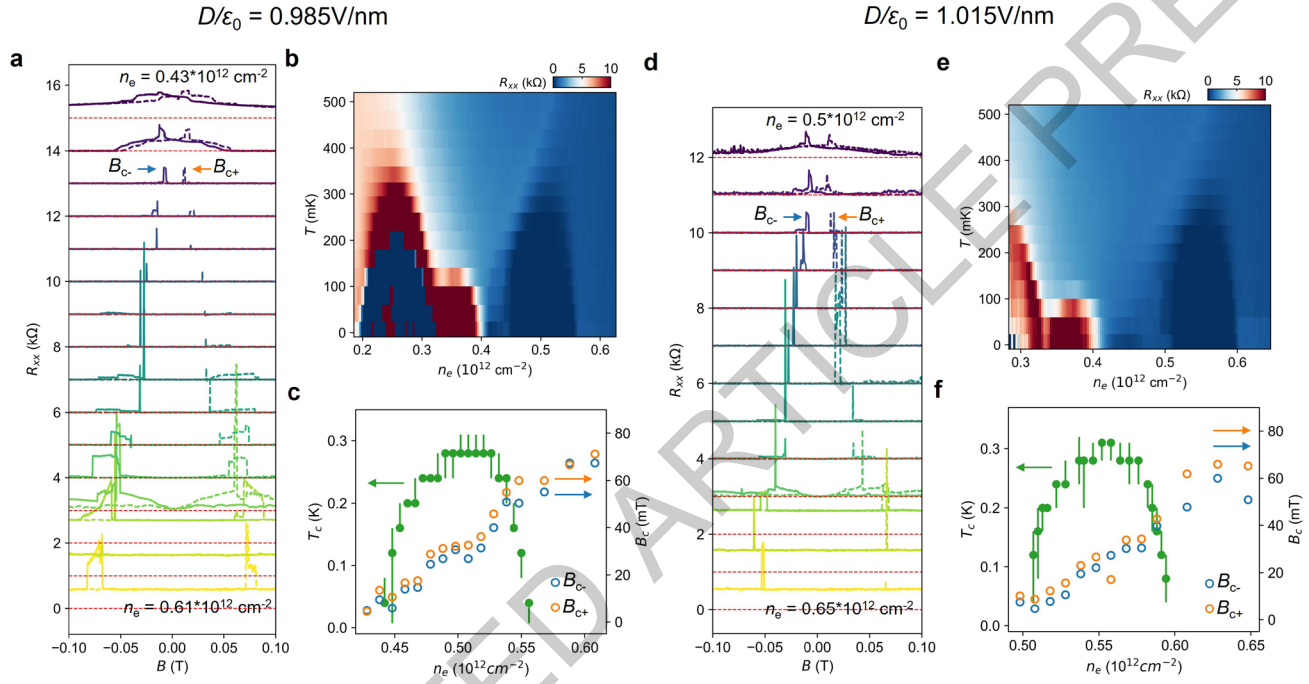
Extended Data Fig. 2

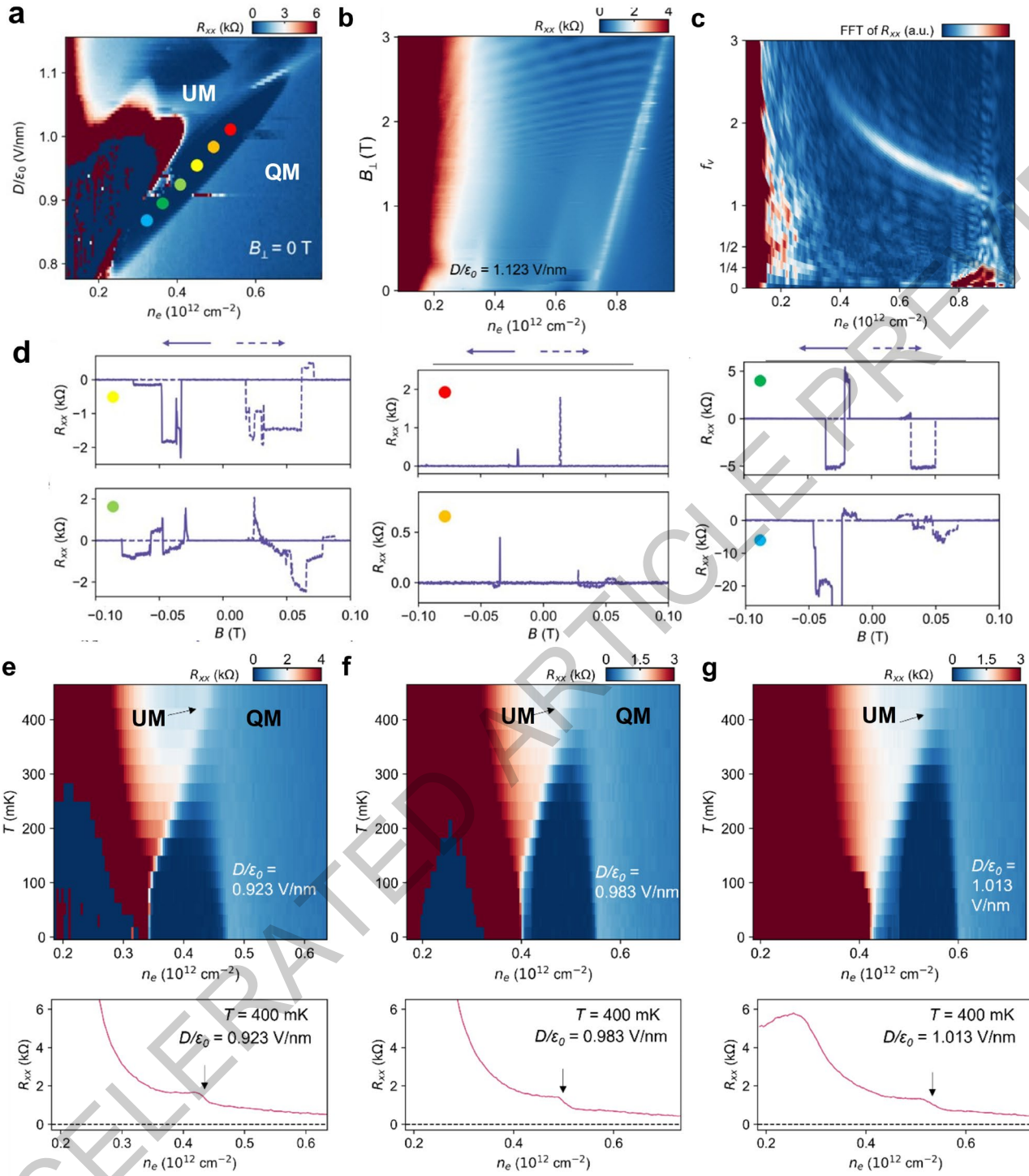


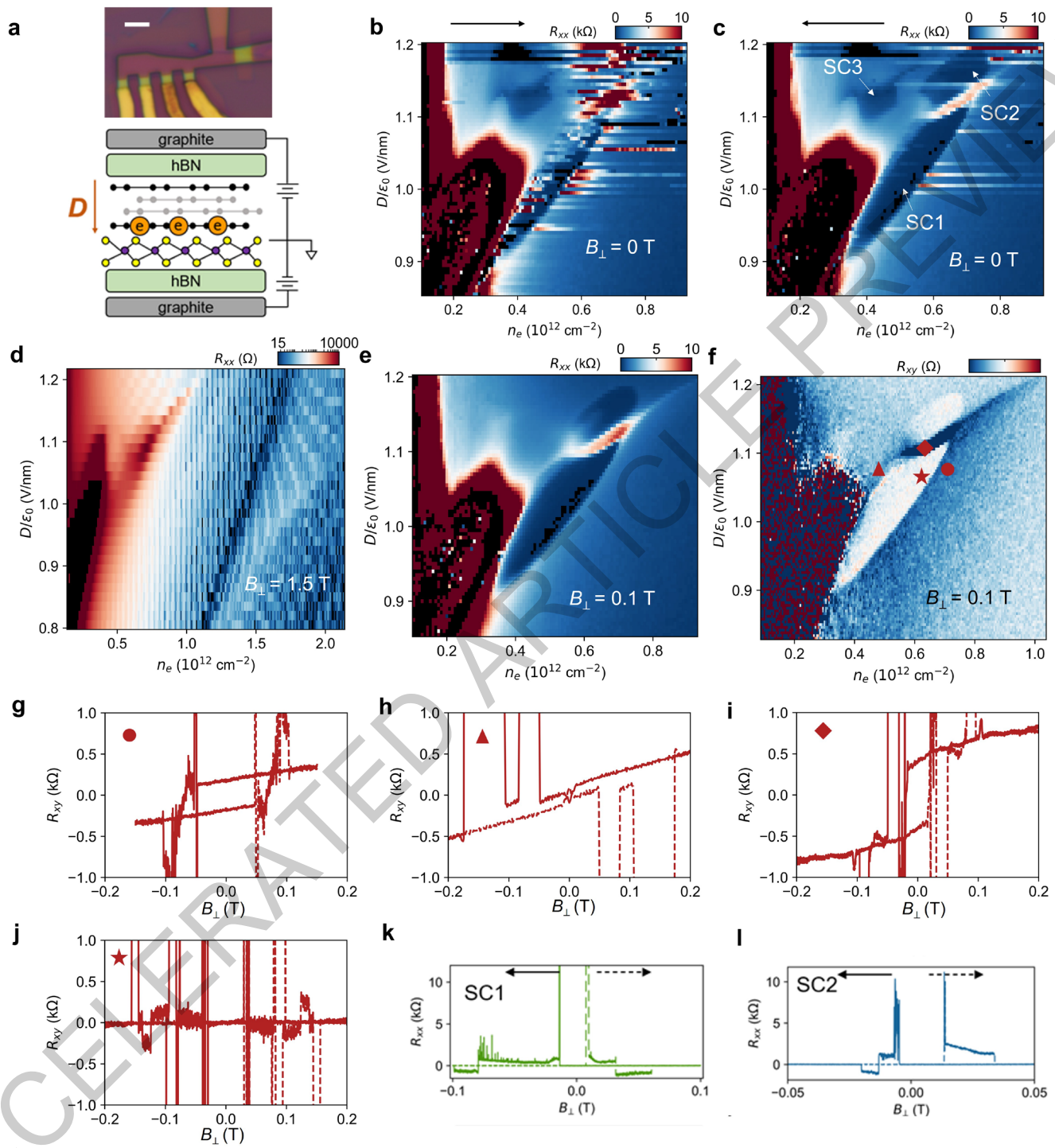
Extended Data Fig. 3



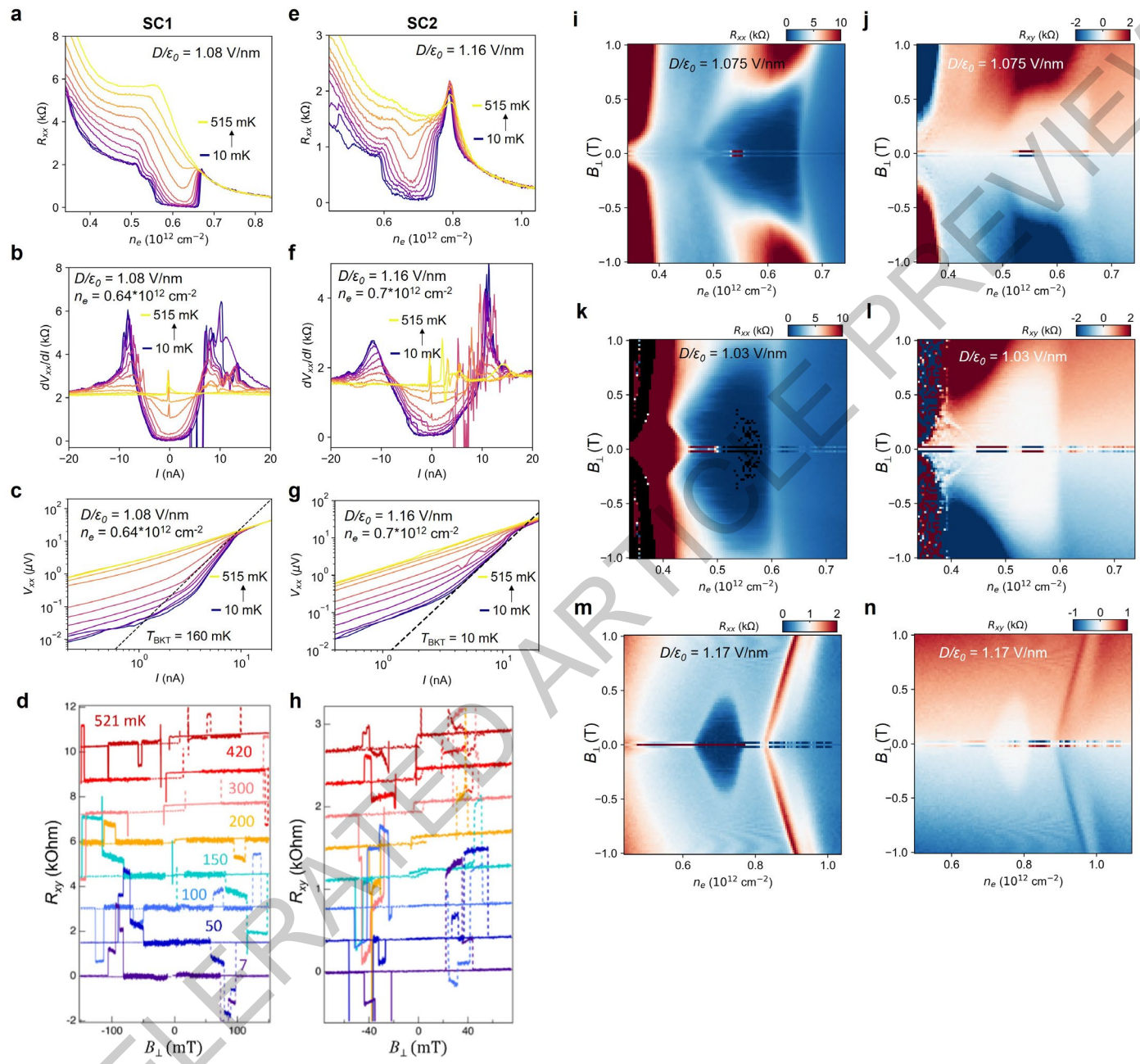
Extended Data Fig. 4



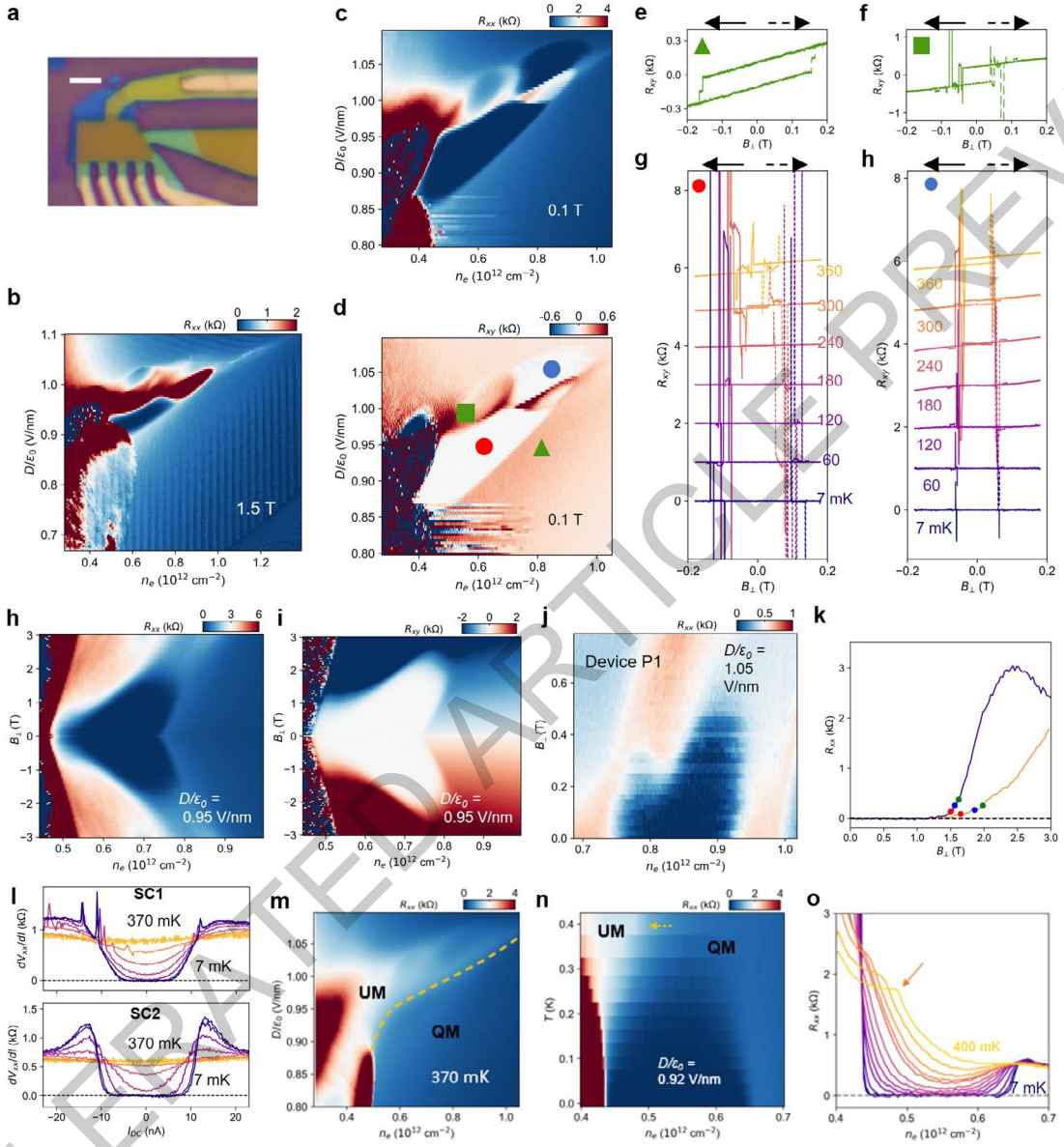




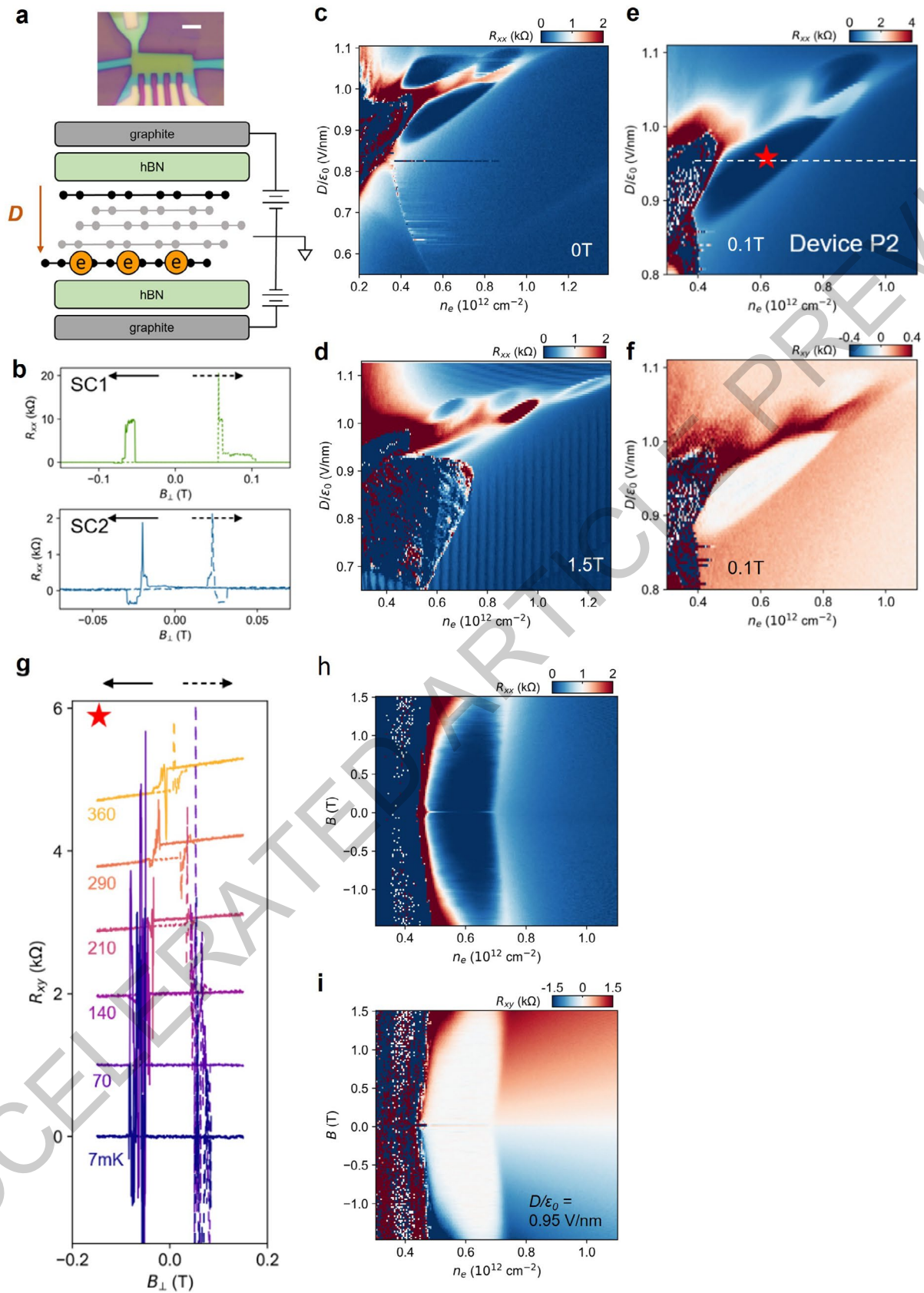
Extended Data Fig. 7



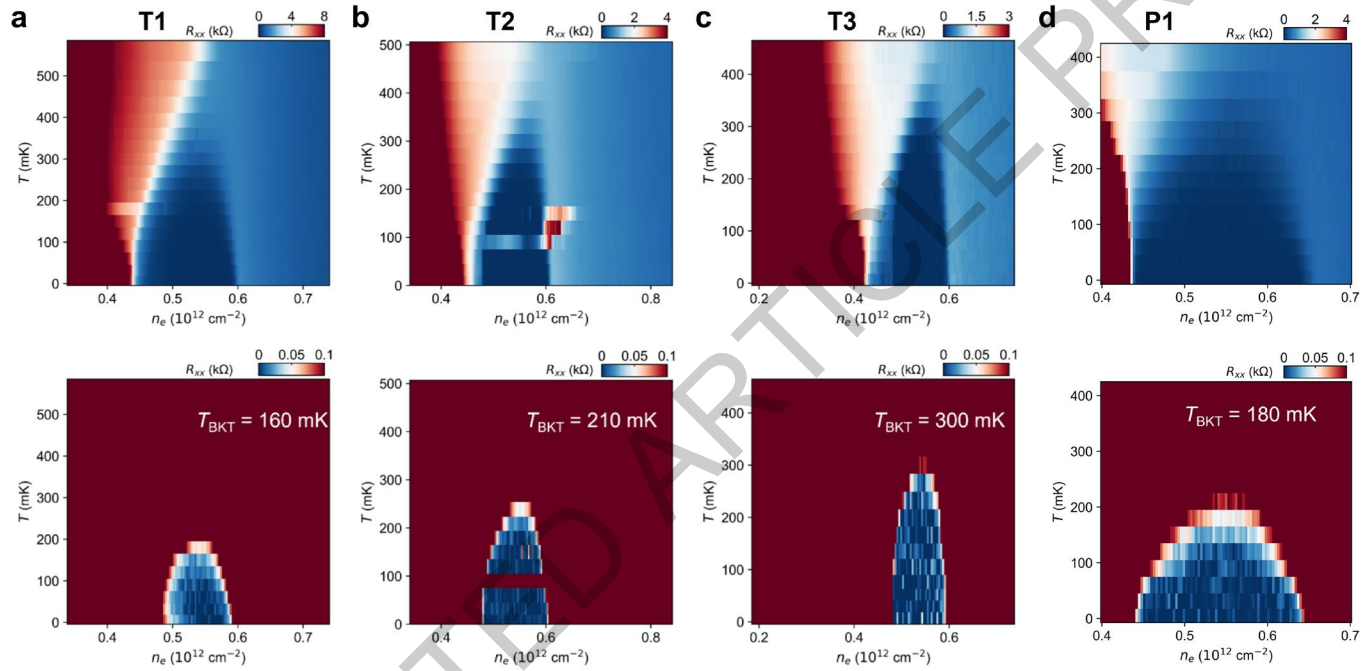
Extended Data Fig. 8



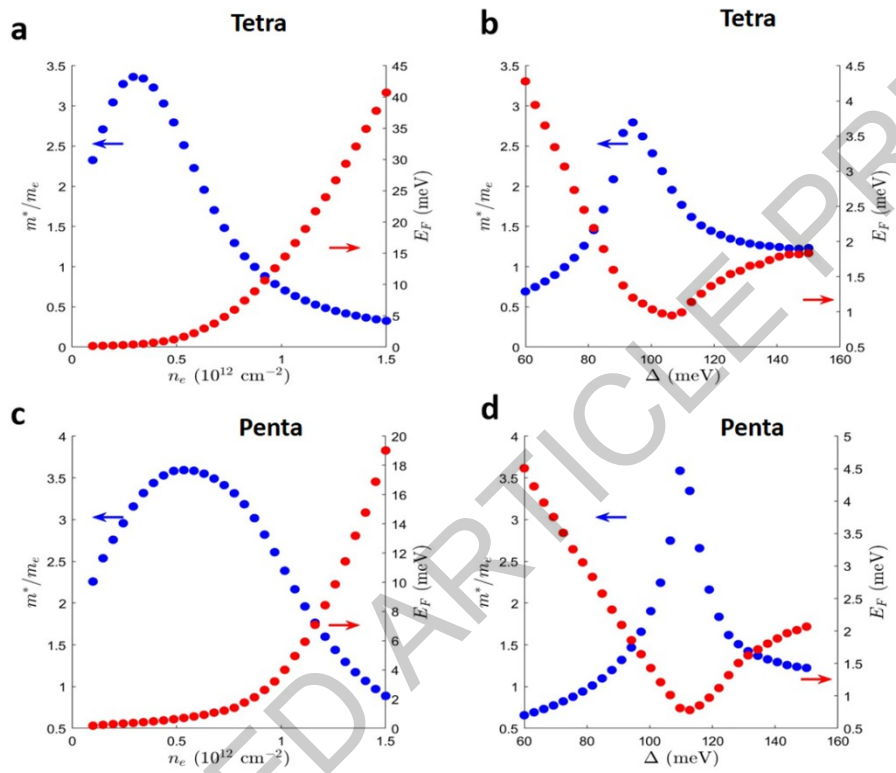
Extended Data Fig. 9



Extended Data Fig. 10



Extended Data Fig. 11



Extended Data Fig. 12